Significant Improvement of Cloud Representation in Global Climate Model MRI-ESM2

Hideaki Kawai[1], Seiji Yukimoto[1], Tsuyoshi Koshiro[1], Naga Oshima[1], Taichu Tanaka[1], Hiromasa Yoshimura[1], Ryoji Nagasawa[1]

[1]Meteorological Research Institute, Japan Meteorological Agency, Tsukuba, 305-0052, Japan

Correspondence to: Hideaki Kawai (h-kawai@mri-jma.go.jp)

Abstract. The development of the climate model MRI-ESM2, which is planned for use in the sixth phase of the Coupled Model Intercomparison Project (CMIP6) simulations, involved significant improvements to the representation of clouds from the previous version MRI-CGCM3, which was used in the CMIP5 simulations. In particular, the serious lack of reflection of solar radiation over the Southern Ocean in MRI-CGCM3 was drastically improved in MRI-ESM2. The score of the spatial pattern of radiative fluxes at the top of the atmosphere for MRI-ESM2 is better than for any CMIP5 model. In this paper, we set out comprehensively the various modifications related to clouds that contribute to the improved cloud representation, and the main impacts on the climate of each modification. The modifications cover various schemes and processes including the cloud scheme, turbulence scheme, cloud microphysics processes, interaction between cloud and convection schemes, resolution issues, cloud radiation processes, interaction with the aerosol model, and numerics. In addition, the new stratocumulus parameterization, which contributes considerably to increased low cloud cover and reduced radiation bias over the Southern Ocean, and the improved cloud ice fall scheme, which alleviates the time-step dependency of cloud ice content, are described in detail.

1 Introduction

Representation of clouds is crucially important for climate models because errors in simulated radiative fluxes are caused mainly by poor representation of cloud rather than by errors in the clear sky radiation calculation. Consequently, biases in clouds are the major factor for biases in the radiation budget and sea surface temperature (SST) that essentially determine the basic performance of climate models. In addition, it is widely recognized that a large part of the uncertainty in projected increases in surface temperature in global warming simulations by climate models arises from large uncertainties in cloud feedback (e.g., Soden and Held, 2006; Soden et al., 2008). To obtain reliable cloud feedback in the climate models used for the projection, clouds must be represented realistically, at least in their climatology. Therefore, cloud schemes and their related processes are the most important atmospheric physical processes to be considered and carefully examined in the development of climate models.

When a climate model undergoes a major upgrade with a new version name, many minor modifications are often included rather than the introduction of a completely new sophisticated scheme. However, details are generally not provided of such minor modifications including the technical information and the tuning of physics schemes related to clouds, although such information is very useful and includes much scientific and technical value. Mauritsen et al. (2012) is one example of a publication that provides practical and honest information for tuning of a climate model.

We participated in the fifth phase of the Coupled Model Intercomparison Project (CMIP5) (Taylor et al., 2012) and the Cloud Feedback Model Intercomparison Project Phase 2 (CFMIP-2) (Bony et al., 2011) using our global climate model, MRI-CGCM3 (Yukimoto et al., 2012, 2011). However, its representation of clouds was unsatisfactory. In the updated version of our climate model, MRI-ESM2 (Yukimoto et al., 2019), which is planned for use in CMIP6 (Eyring et al., 2015) and CFMIP-3 (Webb et al., 2017) simulations, the representation of clouds is significantly improved. The score of the spatial pattern of radiative fluxes for MRI-CGCM3 was worse than the average of the 48 CMIP5 models but the score for MRI-ESM2 is better than any of them. The improvement is particularly pronounced over the Southern Ocean. Trenberth and Fasullo (2010) showed that a significant lack of clouds over the Southern Ocean is a serious problem in most climate models and causes huge biases in shortwave radiative flux there. Although MRI-CGCM3 had this problem with biases that were worse than the average CMIP5 model, the biases are dramatically reduced in the new model, MRI-ESM2.

The problems related to clouds in MRI-CGCM3 cover a broad range of issues. For instance, low cloud cover over the mid-latitude and subtropical oceans is insufficient, the ratio of super-cooled liquid water to cloud (liquid and ice) water is too small, the number concentration of cloud droplets of the Southern Ocean clouds is inadequate, the reflection of solar radiation over the tropics is overestimated, vertical structures of low cloud transition are unrealistic, there are several coding bugs, and ice water content shows strong time-step dependency. To solve these problems and give a better physical basis to the processes, many modifications were implemented in MRI-ESM2. The model update includes:

(i) the introduction of a new stratocumulus parameterization,

(ii) a modified treatment of the Wegener–Bergeron–Findeisen (WBF) process,

(iii) a modified treatment of interaction between stratocumulus and shallow convection,

(iv) an increase in the vertical resolution,

(v) the introduction of a new cloud overlap scheme,

(vi) increased horizontal resolution for the radiation calculation,

(vii) various bug fixes,

(viii) updated aerosol size distributions,

(ix) an improved cloud ice fall scheme.

Item (i) is related to the cloud and turbulence schemes, (ii) to cloud microphysics process, (iii) to interaction between the cloud and convection schemes, (iv) and (vi) to resolution issues, (v) to cloud radiation process, (viii) to the aerosol properties, and (ix) to numerics. Improvements and modifications in this wide range of processes contribute to the improved cloud representation in MRI-ESM2. It is worth describing the main effect of each modification separately with the background of

64 the modification, and such information is very useful for model developers. We would like to emphasize again that the

65 improvement of climate model performance due to updates is ordinarily contributed by the cumulative effect of a lot of

66 modifications, some of which may seem to be minor, rather than by the introduction of a new sophisticated scheme. In this

67 paper, the impacts of each modification are examined by comparing the result of a control AMIP simulation using the new

68 model MRI-ESM2 and results of AMIP experiments in which each updated process is separately turned off.

69   In addition, the new stratocumulus parameterization, which contributes considerably to increased low cloud cover and

70 reduced radiation bias over the Southern Ocean, includes scientifically new concepts, and the improved cloud ice fall scheme,

71 which alleviates the time-step dependency of cloud ice content, includes technically important issues. Therefore, these two

72 items are described in detail in the later section.

73

74

75   2 Models and experiments

76

77   2.1 Models

78   The cloud scheme in MRI-CGCM3 (Yukimoto et al., 2012, 2011; T_L159L48 in the standard configuration) is a two-

79 moment cloud scheme developed and modified from the Tiedtke cloud scheme (Tiedtke, 1993; Jakob 2000). Cloud fraction,

80 cloud liquid water and cloud ice water contents (LWC and IWC), number concentrations of cloud droplets and ice crystals

81 are prognostic variables. The source and sink terms of cloud fraction, LWC, and IWC are calculated basically following

82 Tiedtke (1993): the source terms include formation of stratiform cloud due to upward motion and temperature decrease and

83 detrainment from convection, and sink terms include evaporation. For the temperature range from –38 to 0 ℃, deposition

84 nucleation is calculated based on Meyers et al. (1992), and depositional growth and evaporation for cloud ice are calculated

85 following Rutledge and Hobbs (1983). As processes for freezing of cloud droplets to ice crystals, immersion freezing and

86 condensation freezing (Bigg 1953; Murakami, 1990; Levkov et al., 1992; Lohmann, 2002), and contact freezing (Lohmann

87 and Diehl, 2006; Cotton et al., 1986) are calculated. Conversion of LWC to rain is calculated based on Manton and Cotton

88 (1977) and Rotstayn (2000). Melting of cloud ice and snow occurs just below an altitude where the atmospheric temperature

89 is 273.15 K. In MRI-ESM2 (Yukimoto et al. 2019; T_L159L80 in the standard configuration), all these processes are

90 essentially the same as in MRI-CGCM3. The treatments of stratocumulus, the Bergeron–Findeisen effect, cloud ice fall, and

91 conversion of IWC to snow are discussed later in detail because they are modified from MRI-CGCM3 to MRI-ESM2.

92   Aerosols are calculated by the Model of Aerosol Species in the Global Atmosphere mark-2 revision 4-climate

93 (MASINGAR mk-2r4c) (Yukimoto et al., 2011; Tanaka et al., 2003; Yukimoto et al., 2019), which is coupled to MRI-ESM2.

94 Five species of aerosols are utilized in the cloud and radiation schemes: sulfate, black carbon, organic matter, sea salt (2 size

95   modes), and mineral dust (6 size bins). The activation of aerosols into cloud droplets is calculated based on Abdul-Razzak et

96   al. (1998), Abdul-Razzak and Ghan (2000), and Takemura et al. (2005). The ice nucleation for cirrus clouds is calculated

97   using a parameterization of Kärcher et al. (2006), including homogeneous nucleation (Kärcher and Lohmann, 2002) and

98   heterogeneous nucleation (Kärcher and Lohmann, 2003).

99

2.2 Basic performance

101   First, we briefly show improvements from MRI-CGCM3 to MRI-ESM2 in the basic performance of the simulations.

102   Figure 1 shows the total cloud cover and its bias in the present-day climate from the historical simulations using MRI-

103   CGCM3 and MRI-ESM2. Observational data for total cloud cover (Pincus et al., 2012; Zhang et al., 2012) that are derived

104   from the International Satellite Cloud Climatology Project (ISCCP; Rossow and Schiffer, 1999) D1 data and radiative flux

105   observational data from the Clouds and Earth's Radiant Energy Systems (CERES) Energy Balanced and Filled (EBAF; Loeb

106   et al., 2009) product are used as observational climatologies. It is clear that total cloud cover simulated by MRI-CGCM3 is

107   much less than the observations, especially over the Southern Ocean and subtropical oceans off the west coast of the

108   continents. However, total cloud cover is substantially increased in the simulation using MRI-ESM2 over these areas and the

109   bias is reduced significantly. As a result, a large negative bias in the upward shortwave radiative flux at the top of the

110   atmosphere (TOA) found in MRI-CGCM3 is reduced substantially in the simulation using MRI-ESM2. In addition, a

111   positive bias in the tropics is also reduced.

112   Figure 2 shows the Taylor diagrams (Taylor, 2001) for upward shortwave, longwave, and net radiative fluxes from the

113   48 CMIP5 models. The scores of spatial patterns of shortwave, longwave, and net radiative fluxes for MRI-CGCM3 are near

114   or worse than the average among the 48 CMIP5 models, but the scores for MRI-ESM2 are better than any of the models. The

115   scores for MRI-ESM2 are even almost comparable to the scores of the ensemble mean of CMIP5 models. Although the

116   uncertainty in the observational data for cloud radiative effect is larger than that of radiative fluxes at the top of the

117   atmosphere, the scores of cloud radiative effect for shortwave, longwave, and net radiation show similar characteristics to the

118   corresponding scores for TOA radiative fluxes (Fig. S1). This implies that improvement of TOA radiative fluxes in MRI-

119   ESM2 can be attributed to improvement of cloud representation in the model.

120

2.3 Experiments

122   The purpose of this paper is to identify the effect of each modification applied to the model under controlled conditions

123   in order to understand the significant improvement of the radiative flux in the new model. Therefore, we chose AMIP

124   simulations to avoid being influenced by changes in SST. A series of experiments with the new model MRI-ESM2 is

125   performed, with each modification summarized in Sect. 1 in turn set to the old (MRI-CGCM3) treatment. A list of sensitivity

126 experiments performed in the present study using MRI-ESM2 is given in Table 1. We ran the model from 2000 to 2010 and

127 used the data for 10 years from 2001 to 2010 for analysis.

128

129

3 Updates and their impacts

131   In this section, the updates from various aspects are explained with their backgrounds. The main impact of each update

132 is shown and discussed based on the comparison between the results of the updated new model and the experiments in which

133 each modification in turn is turned back to the old treatment.

3.1 New stratocumulus parameterization

135   Representation of low clouds including stratocumulus in climate models has been one of the most bothersome problems

136 for many years (e.g., Duynkerke and Teixeira, 2001; Siebesma et al., 2004), and low clouds are poorly reproduced even in

137 the state-of-the-art climate models (e.g., Nam et al., 2012; Su et al., 2013; Caldwell et al., 2013; Koshiro et al., 2018). As a

138 result, solar reflectance by clouds has significant negative biases over areas frequently covered by stratocumulus (e.g.,

139 Trenberth and Fasullo, 2010; Li et al., 2013). A new stratocumulus scheme that utilizes a stability index that takes into

140 account the effect of cloud top entrainment (Kawai et al., 2017) was introduced instead of the old stratocumulus scheme

141 (Kawai and Inoue, 2006). A detailed description and physical interpretation are given in Sect. 4. Figure 3 shows that low

142 cloud cover increases significantly in the subtropical oceans off the west coast of the continents and over the Southern Ocean,

143 which is a significant result of upgrading the stratocumulus scheme. Low cloud cover is increased by more than 20% over

144 the oceans off California, Peru, Namibia, and west coast of Australia, and by more than 10% over the Southern Ocean. As a

145 result, upward shortwave radiative flux (reflection of solar insolation) also increases and this impact contributes to reducing

146 the large bias in shortwave radiative flux over these regions.

147

3.2 Treatment of the WBF effect

149   In recent years, several studies (e.g., McCoy et al., 2015; Cesana and Chepfer, 2013) revealed that ratios of super-

150 cooled liquid water with respect to cloud (liquid + ice) water in climate models are much lower than those in the Cloud–

151 Aerosol Lidar and Infrared Pathfinder Satellite Observations (CALIPSO; Winker et al., 2009) data (e.g., Hu et al., 2010;

152 Cesana and Chepfer, 2013). Some studies pointed out that the lack of super-cooled liquid water in climate models is the

153 source of insufficient solar reflectance of clouds over the Southern Ocean (e.g., Bodas-Salcedo et al., 2016; Kay et al., 2016).

154 Liquid clouds are optically thicker than ice clouds if the cloud (liquid + ice) water content is the same, because the size of

cloud droplets is much smaller than that of ice crystals and this corresponds to larger number concentration for cloud droplets.

The WBF process is a deposition growth process of ice crystals at the expense of cloud droplets due to ice saturation being lower than liquid water saturation. The WBF effect was treated in a way similar to Lohmann et al. (2007) in MRI-CGCM3. When IWC is greater than a threshold of 0.5 mg kg^{-1}, all super-cooled water in the grid box is forced to evaporate within the time step and all source terms for LWC are set to zero. However, this treatment caused excessive evaporation of super-cooled water. In MRI-ESM2, when IWC exceeds the threshold, only the part of LWC that corresponds to the depositional growth of ice crystals is evaporated within the time step. In addition, the source terms of LWC are not ignored but calculated in a proper fashion. However, there is an arbitrariness about how these source terms are divided into the source terms of LWC and IWC. The first reason for the arbitrariness is that the time step of our climate models is too long (30 minutes) to resolve cloud microphysics and a part of the generated liquid water can change to ice crystals within this time step, especially when IWC exceeds the threshold. The second reason is that the liquid water and ice water are assumed to be well mixed in the model grid box if they coexist, as in most global climate models. However, there should be mixed phase parts, ice only parts, and liquid only parts in a volume corresponding to the model grid box size (Tan and Storelvmo 2016). Therefore, it is difficult to determine the LWC–IWC partitioning of the source terms theoretically. We decided to use a ratio derived by Hu et al. (2010) based on satellite observations to determine the ratio of the source terms into LWC and IWC only when the WBF effect occurs, that is, when IWC is greater than the threshold. This is an empirical and simple method, but this treatment can supplement the defects of the modelled microphysics due to the uncertainty and complexity by utilizing observational data.

Figure 4 shows the ratio of super-cooled liquid water in clouds as a function of temperature in the simulations using new and old treatments of the WBF effect. It is clear from the figure that the ratio of super-cooled liquid water is significantly increased in the new treatment and close to the satellite observations of Hu et al. (2010); the ratio at 255 K is increased from 52% to 84% for the mass-weighted ratio and from 18% to 78% for the frequency ratio. Both mass-weighted ratio and frequency ratio, which should correspond to the ratio derived from satellite observations, using the new treatment are close to the satellite observations. In MRI-ESM2, IWC production from the source terms of LWC based on partitioning using a function of Hu et al. (2010) is dominant, and the contributions from a depositional growth and other freezing processes are considerably small. Figure 5 shows the impact of the new treatment of the WBF effect on TOA upward shortwave radiative flux. The reflection of solar insolation is significantly increased over the Southern Ocean using the new treatment (Fig. 5), and consequently, this new treatment contributes considerably to the reduction in shortwave radiation bias over the area shown in Fig. 1. The increase in the ratio of super-cooled liquid water in MRI-ESM2 plausibly contributes to the higher climate sensitivity in the model than in MRI-CGCM3, because an increased ratio of super-cooled liquid water weakens the cloud-phase feedback that negatively contributes to cloud feedback (Tsushima et al., 2006; McCoy et al., 2015; Bodas-Salcedo et al., 2016; Kay et al., 2016; Tan et al., 2016; Frey and Kay, 2018).

However, since the new treatment of the WBF effect is still rather simple, it cannot represent observed layered structures with a thin super-cooled water layer at the top of cloud layers and ice layer below (Forbes and Ahlgrimm, 2014; Forbes et al., 2016). In addition, it is possible that the curve of Hu et al. (2010) over-estimates the ratio of super-cooled liquid water (Cesana and Chepfer, 2013; Cesana et al., 2016). It should also be noted that empirical relationships including the ratio curve of Hu et al. (2010) may not hold completely in a future climate because a large number of meteorological factors contribute to form such relationships and they may change in a systematic way. Therefore, more sophisticated treatments need to be developed in the future.

3.3 Interaction between stratocumulus and shallow convection

It is well-known that the altitude of the low-level cloud layer gradually increases westward in subtropical stratocumulus regions, including off Peru, in association with the transition from stratocumulus to cumulus (Bretherton et al., 2010; Rahn and Garreaud, 2010; Abel et al., 2010; Kawai et al., 2015). However, the vertical structures of the transition were unrealistically discontinuous in the old model as seen in Fig. 6b. This discontinuity was caused by an unrealistically formed temperature inversion just above the stratocumulus-like cloud layer due to excessive adiabatic heating by the convection scheme that activates shallow convection in those regions. Therefore, in the new version, the occurrence of shallow convection is prevented over the area where the conditions for stratocumulus occurrence (See Section 4.1 in more detail) are met. As a result, the vertical structures of low-level clouds are significantly improved, as seen in Fig. 6a. Such a switch for shallow convection is sometimes used in atmospheric models, although it is a simple and practical method. For example, a threshold of estimated inversion strength (EIS; Wood and Bretherton, 2006) is used to determine the activation of shallow convection in version CY43r3 of the European Centre for Medium-Range Weather Forecasts (ECMWF) Integrated Forecast System (IFS) (ECMWF, 2017).

3.4 Vertical resolution

The thickness of observed stratocumulus is typically 200−300 m (Wood 2012), but can be as thin as 50 m during the daytime, especially in the Californian stratocumulus region (Betts, 1990; Duynkerke and Teixeira, 2001). The model vertical resolution was increased from L48 (48 vertical levels) in the MRI-CGCM3 to L80 in the MRI-ESM2 (Yukimoto et al. 2019), and the number of vertical layers in the atmospheric boundary layer was nearly doubled (from 5 to 10 layers below 900 hPa). As seen in Fig. 6c, the low cloud layer can be geometrically too thick in the model with resolution L48, which can cause too high an albedo, because the vertical layer thickness is about 300 m at the level of 900 hPa and this is the minimum thickness of clouds that can be represented in the model. Sensitivity of represented stratocumulus to model vertical resolution has been widely reported (Teixeira, 1999; Bushell and Martin, 1999; Wang et al., 2004; Wilson et al., 2008; Neubauer et al., 2014; Guo et al., 2015). Although several methods that compensate for insufficient vertical resolution have been developed,

220 including the use of vertical sub-levels (Wilson et al. 2007) and the introduction of areal cloud fraction, which is different

221 from volume cloud fraction (Brooks et al., 2005), we decided for the moment not to introduce those methods for simplicity

222 and consistency in the model physics.

223

3.5 Cloud overlap

225   In the longwave radiation scheme, maximum-random overlap (Geleyn and Hollingsworth, 1979) is adopted as a cloud

226 overlap assumption. In contrast, in the shortwave radiation scheme, total cloud cover in a column (the cloudy area) is first

227 calculated based on maximum-random overlap, and second, random overlap is adopted indirectly to calculate multiple

228 scattering in the cloudy area in the MRI-CGCM3 (Yukimoto et al., 2011, 2012). However, the inadequate treatment of the

229 cloud overlap assumption in the shortwave radiation scheme causes overestimation of the reflection of incident solar

230 radiative flux, especially for tower-shaped cumulus clouds with optically thin high-level clouds (e.g. anvil) (Nagasawa,

231 2012). In MRI-ESM2, because a practical independent column approximation (PICA; Nagasawa, 2012) based on Collins

232 (2001) was implemented, the maximum-random overlap became available in the shortwave radiation scheme. Application of

233 the maximum-random overlap in the shortwave radiation scheme significantly decreased the reflection of shortwave

234 radiative flux over the tropical convection areas without varying total cloud cover (Fig. 7). This reduction makes a

235 significant contribution to reduce the excessive reflection of incident shortwave radiative flux over the tropics (see Fig. 1).

236

3.6 Horizontal resolution for radiation calculation

238   The computational cost for radiation calculation is heavy in climate models and this cost was reduced in MRI-CGCM3

239 by reducing the radiation calculation spatially and temporally. Full radiation computations were performed for every two

240 grid boxes in the zonal direction, and shortwave and longwave radiation was calculated 1-hourly and 3-hourly, respectively.

241 Figure 8 shows the impacts of increased horizontal resolution for the radiation calculation (calculation for every single grid)

242 (Fig. 8a, 8b) and increased frequency of calculation (1-hourly calculation) for longwave radiation (Fig. 8c, 8d). In both cases,

243 low-level clouds in the subtropics off the west coasts of the continents and at mid-latitudes increased, increasing shortwave

244 reflectance a little. This increase in low cloud cover can be attributed to improved cloud–radiation interactions: cloud-top

245 longwave cooling of low clouds, which is the primary physical process to maintain low clouds (e.g., Wood 2012), is

246 consistently calculated at the top of existing low clouds without spatial smoothing and temporal inconsistency. Either

247 modification is physically appropriate and improves the representation of low clouds. However, the total computational cost

248 was increased by 5% for the spatial resolution modification and by 10% for the temporal resolution modification.

249 Considering cost and merit comprehensively, we decided to adopt the modification only for the spatial resolution and keep

250 the temporal treatment unchanged.

251

3.7 Bug fixes

No climate models are free from coding bugs, and they sometimes exert significant impacts on model results, although they are rarely documented in publications. MRI-CGCM3 also had some bugs that affect the simulation results to some extent. One of them is associated with the prognostic equations for number concentrations of the cloud particles. This bug caused a problem of large number concentrations of cloud particles leading to excessive optical thickness and accompanying excessive reflection of solar radiation, particularly for stratocumulus and stratus over the subtropics and northern Pacific region (Tsushima et al., 2016). In addition, the bug caused a large decrease in the number concentration of cloud droplets and large positive cloud feedback for such clouds in warmer climate simulations (Kawai et al. 2015). Several bugs including this serious bug were fixed in MRI-ESM2.

3.8 Aerosol size distributions

Our climate models calculate number concentrations of aerosols from the mass concentrations using the prescribed aerosol size distributions, and the number concentrations are used to calculate number concentrations of cloud particles. Therefore, an appropriate treatment of the aerosol size distributions is important to estimate the aerosol effect on clouds. Aerosol size distributions, namely the geometric mean radius and standard deviation in lognormal size distribution, were modified in MRI-ESM2 based on recent observations. For example, the increase in the geometric mean radius of organic carbon from 0.0212 (Chin et al., 2002) to 0.1 μm (Seinfeld and Pandis, 2006; Liu et al., 2012) in MRI-ESM2 causes a significant decrease in the number concentration of cloud particles that originate from organic carbon. This modification significantly decreases the response of cloud optical thickness to assumed changes in the emission of organic carbon. On the other hand, the mode radius of fine mode sea salt is decreased from 0.228 (Chin et al., 2002) to 0.13 μm (Seinfeld and Pandis, 2006) and the change causes higher number concentration of cloud droplets originating from sea salt. In addition, the number concentration of cloud condensation nuclei (CCN) originating from fine mode sea salt is multiplied by a factor of 2.0 after the calculation from the number concentration of sea salt. This treatment is introduced because we use only two size modes (i.e., fine accumulation and coarse modes) of sea salt and the model cannot represent sea salt in the Aitken mode, although a part of the sea salt in Aitken mode can work as CCN. Actually, the number concentration of sea salt in Aitken mode is difficult to estimate from the mass concentration of aerosols because they contribute substantially to the number but contribute little to the mass. To represent the contribution of sea salt in Aitken mode to CCN in a simple way, the factor of 2.0 is multiplied as a provisional solution until sea salt in Aitken mode can be calculated explicitly. This factor is estimated from observational studies (e.g., Covert et al., 1996; Clarke et al., 2006). In fact, a lower limit of the number concentration of cloud droplets has been used in a significant number of state-of-the-art climate models to prevent too small number concentrations of cloud droplets in clean air conditions (Hoose et al., 2009; Jones et al., 2001; Lohmann et al., 2007; Takemura et al., 2005). However, it is pointed out that this lower limit drastically controls the magnitude of the aerosol

284 indirect effect, for instance, measured as the difference between present-day and preindustrial climates (Hoose et al., 2009).

285 Therefore, the lower limit of cloud droplets is not introduced in our model. We believe that our treatment is better than

286 introducing a lower limit of cloud droplets although it is quite simple, because the treatment has a more physical basis. This

287 treatment increases cloud droplet number concentration by more than 30% and also increases reflection of shortwave

288 radiation by 4 W m^{-2} over the Southern Ocean (Fig. 9).

289

3.9 Ice sedimentation and ice conversion to snow

291   The method for calculating cloud ice sedimentation in the MRI-CGCM3 was not sophisticated, and it caused unrealistic

292 ice sedimentation and strong time-step dependency of IWC. While IWC is a prognostic variable in the MRI-CGCM3, snow

293 is not but it is treated as snow flux in the model. A part of IWC is diagnosed as snow and removed from the IWC at each

294 time step and falls down to the surface within one time step. The main problem was that the ratio of snow was not

295 proportional to the time step. As a result, a substantial amount of snow is repeatedly removed from IWC when the time step

296 is shortened. To solve the problem, the treatment of cloud ice sedimentation and conversion of cloud ice to snow was

297 improved based on the study of Kawai (2005). Figure 10 shows that IWC is large for a time step of 3600 s but monotonically

298 decreases with shorter time steps. On the other hand, IWC is not affected by the time step in the control simulation that uses

299 the modified scheme of ice sedimentation and ice conversion to snow. A detailed description of the modification is given in

300 Sect. 4, because this modification contains some important insights and solutions related to the numerical issues.

301

3.10 Summary of impacts on shortwave radiative flux

303   Figure 11 summarizes the impacts of each modification on zonal means of low cloud cover and TOA upward

304 shortwave radiative flux. The new stratocumulus scheme contributes to an increase in low cloud cover mainly over the

305 Southern Ocean, and the suppression of shallow convection under stratocumulus conditions contributes a low cloud cover

306 increase over the mid-latitudes in the Southern Hemisphere. Increased horizontal resolution in the radiation calculation

307 additionally contributes to the low cloud cover increase. The increase in reflection of solar radiation over the Southern Ocean

308 and mid-latitudes in the Southern Hemisphere is largely contributed by the new stratocumulus scheme, the new treatment of

309 the WBF effect (especially around 60°S), the doubled number concentration of sea salt CCN, and the treatment of shallow

310 convection suppressed under stratocumulus conditions (over latitudes lower than the areas impacted by other modifications).

311 The new treatment of the WBF effect and doubled number concentration of sea salt CCN increase the reflection of solar

312 radiation by increasing cloud optical thickness. A new cloud overlap scheme, PICA, contributes to reduction in solar

313 radiation reflection over the tropics without changing the cloud cover. These modifications in MRI-ESM2 significantly

314 reduce the large bias in the solar radiation reflection present in MRI-CGCM3, which is negative over the Southern Ocean

315 and positive over the tropics (Fig. 1e, 1f, and Fig. 11c). Note that the significant improvement in the shortwave radiative flux

316 is not attributed to the introduction of a new advanced scheme but to the cumulative effect of many minor modifications.

317

3.11 Comments on tuning

319   At the end of this section, we give a brief description of the model tuning related to clouds. At a stage of developing

320 schemes, a number of amip type simulations (with typical one-year length) were performed using atmospheric and aerosol

321 coupled model, to check the basic behavior of schemes and the basic impacts on radiative fluxes. At a tuning stage, five-year

322 runs of amip type simulations were mainly examined. The main targets for tuning parameters related to clouds in MRI-

323 ESM2 were global-mean biases and root-mean square errors of shortwave and longwave radiative fluxes at the top of the

324 atmosphere. The tuning parameters related to clouds are parameters which affect differently by cloud types and control cloud

325 properties such as cloud cover, cloud water content, and cloud number concentration. In the stratocumulus parameterization

326 (Section 3.1), the threshold value of ECTEI was tuned to increase Southern Ocean clouds as described in Section 4.1.3. The

327 relatively large mode radius of sulfate of 0.10 μm (possible range: 0.05 – 0.10 μm) was chosen to obtain smaller cloud

328 droplet number concentration to prevent an excessive aerosol-cloud interaction. Treatment of the WBF effect (Section 3.2),

329 cloud overlap scheme (Section 3.5), schemes for ice sedimentation and ice conversion to snow (Section 3.9), and others

330 (Sections 3.3, 3.4, 3.6, and 3.7) were not tuned. Descriptions of the model tuning (other than cloud-related parameters) are

331 given in Yukimoto et al. (2019).

332

4 Detailed description of schemes

334   In this section, modifications and improvements in two schemes are explained in detail, because they include

335 scientifically new concepts and technically important insights and solutions related to the numerical issues; one is the new

336 stratocumulus parameterization and the other is the improved cloud ice fall scheme.

4.1 New stratocumulus parameterization

4.1.1 Old parameterization and problems

339   In the MRI-CGCM3, a stratocumulus scheme slightly modified from Kawai and Inoue (2006), originally developed

340 from Slingo (1980, 1987), was used to represent subtropical stratocumulus. In that scheme, stratocumulus is formed when

341 the following four conditions are met: (i) there is a strong inversion above the model layer, (ii) the layer near the surface is

342 not stable (to guarantee existence of a mixed layer), (iii) the model layer height is below the level of 940 hPa, and (iv) the

343 relative humidity of the model layer exceeds 80%. When all of these conditions are met, cloud cover is determined as a

344 function of the inversion strength, in-cloud cloud water content is determined to be proportional to the saturation specific

345 humidity, and the vertical mixing at the top of the cloud layer is reduced to approximately zero to prevent excess cloud top

346 entrainment.

347   Although this scheme can reproduce subtropical stratocumulus and the cloud radiative effect relatively well, it has

348 several problems. First, it does not give enough low clouds over mid-latitude oceans, especially the Southern Ocean. Low

349 clouds off the west coast of the continents, including off California, off Peru, and off Namibia, are also insufficient,

350 especially areas far from the coast. The second problem is related to the use of inversion strength in parameterization in

351 climate models, which is calculated from the difference of potential temperature between two adjacent vertical model layers.

352 Climate models cannot reproduce realistic strong inversions because their vertical resolution is totally insufficient.

353 Furthermore, the inversion strength reproduced in climate models strongly depends on the model vertical resolution.

354 Therefore, the parameter has to be tuned for each model, if the inversion strength is directly utilized in the parameterization.

355 In addition, there is a strong positive feedback between cloud fraction of low cloud and the inversion strength at the top of

356 the cloud. The positive feedback makes it difficult to utilize inversion strength in the parameterization of low cloud fraction.

357 The third problem is that the vertical structure with a smooth transition from stratocumulus to cumulus cannot be reproduced

358 because the parameterization is limited to below the level of 940 hPa (see Kawai and Inoue, 2006). To solve these problems,

359 we decided to utilize a criterion that represents the structure of the lower troposphere as a whole ("non-local") rather than a

360 detailed local vertical structure.

361 **4.1.2 New index for low cloud cover**

362   Estimated inversion strength (EIS; Wood and Bretherton, 2006), which is a modification of lower tropospheric stability

363 (LTS; Klein and Hartmann 1993), is an index that correlates well with low cloud cover and has been used in many studies.

364 However, EIS takes into account only the temperature profile and does not include information on water vapour. Kawai et

365 al. (2017) developed an index for low cloud cover, the estimated cloud-top entrainment index (ECTEI). This index is

366 deduced from a criterion of cloud top entrainment (Randall, 1980; Deardorff, 1980; Kuo and Schubert, 1988; Betts and

367 Boers, 1990; MacVean and Mason, 1990; MacVean, 1993; Yamaguchi and Randall, 2008; Lock, 2009) and includes

368 information on both the vertical profile of temperature and that of water vapour. The definition of ECTEI is as follows:

369
$$\text{ECTEI} \equiv \text{EIS} - \beta L / c_p (q_{\text{surf}} - q_{700})$$

370 where L is latent heat, c_p is the specific heat at constant pressure, q_{surf} and q_{700} are the specific humidity at the surface and

371 700 hPa, respectively, $\beta = (1 - k) \, C_{\text{qgap}}$, C_{qgap} is a coefficient (= 0.76), and k is a constant (= 0.70; MacVean and Mason

372 1990).

373   Figure 12 shows the climatologies of low stratiform cloud cover and the stability indexes, LTS, EIS, and ECTEI, for

374 December to February and June to August. Cloud cover data were obtained from shipboard observations, the extended edited

375 cloud report archive (EECRA; Hahn and Warren, 2009), and stability indexes were calculated using the ECMWF 40-year

376 Re-Analysis (ERA-40) data (Uppala et al., 2005) for 1957–2002. The definition of low cloud cover (LCC) in the

377 observations is the combined cloud cover of stratocumulus, stratus, and sky-obscuring fog, which is the same conventional

definition as employed in Klein and Hartmann (1993) and Wood and Bretherton (2006). When LCC and LTS maps are compared, the contrast between the subtropics and mid-latitudes is different. LTS is weighted more over the subtropics than over mid-latitudes while LCC is dominant over mid-latitudes. In EIS maps, the value is more weighted in mid-latitudes than in the subtropics, compared with LTS, and the EIS geographical patterns are closer to LCC patterns than LTS patterns, as it is well-known that EIS corresponds to LCC better than LTS. In ECTEI maps, the weight is even larger in mid-latitudes than for EIS and the ECTEI geographical patterns are even closer to LCC patterns than the EIS patterns. These characteristics suggest that EIS does not adequately represent the large occurrence of low cloud over cold oceans including the Southern Ocean and ECTEI can be more appropriate for representation of LCC. Figure 13 shows the relationships between the LCC and the stability indexes, LTS, EIS, and ECTEI. It shows that ECTEI has the best correlation with LCC with correlation coefficients $R = 0.23$ for LTS, $R = 0.83$ for EIS, and $R = 0.90$ for ECTEI.

4.1.3 New parameterization and improvements

In our new scheme, the relationship between ECTEI and LCC is not directly used but ECTEI is used as a threshold of a treatment in the turbulence scheme. In our climate models, vertical smoothing of vertical diffusivity is employed to represent simply the mixing effect due to cloud top entrainment and part of the mixing due to shallow convection. In MRI-ESM2, if ECTEI is larger than a threshold value, the smoothing is prevented, which means the turbulence at the top of the boundary layer is suppressed, and the lower limit of vertical diffusivity is set to a much smaller value (virtually zero) than the original one. This means that cloud top entrainment in the model is switched on and off depending on an ECTEI threshold. In the original setting, the threshold value was set to 0 K and the condition of not stable near-surface layer (to guarantee existence of a mixed layer) was imposed (Kawai 2013). However, after model tuning, the threshold value of ECTEI was set to −2.0 K (possible range: −3.0 − +3.0 K), and the condition of mixed layer existence was removed to apply the suppression of cloud top mixing not only to stratocumulus conditions but also to advection fog conditions, where the near-surface layer is stable. The introduction of this scheme has led to an increase in low cloud cover, especially over the mid-latitude ocean, including the Southern Ocean, and the radiation bias is significantly reduced (Fig. 3).

The application of a condition that represents the detailed local vertical structure may appear to be more physically based than a "non-local" condition. However, parameterizations based on local vertical structures are not appropriate in some cases where (i) model resolution is not sufficient to represent the detailed physical process or (ii) the feedback between the parameters and the variables that should be obtained is very strong. In such cases, the parameters that represent the whole structure of the lower troposphere can produce more robust and reasonable results, although empirical relations are required to construct "non-local" parameterizations.

4.1.4 Brief discussion on climate change simulations

It is well-known that changes in LCC in warmer climates cannot be explained by changes in LTS (e.g., Williams et al., 2006; Medeiros et al., 2008; Lauer et al., 2010). The mechanism of this discrepancy is also well-understood; inevitable

410 decrease of moist adiabatic lapse rate in the free atmosphere in warmer climates causes increase in LTS (e.g., Miller, 1997;
411 Larson et al., 1999), even though the inversion strength that probably contributes to determine LCC does not change (e.g.,
412 Wood and Bretherton, 2006; Caldwell and Bretherton, 2009). It was expected that an index EIS could avoid this problem and
413 could be used for discussion of LCC changes under warmer climates because EIS is a more physics-based index that
414 represents inversion strength at the cloud top more directly. However, more recently, it turned out that LCC tends to decrease,
415 although EIS increases in warmer climates in most climate models (e.g., Webb et al., 2013). Subsequently, it was shown by
416 Qu et al. (2014) that changes (including variations in the present climate and future changes) in LCC can be determined by a
417 linear combination of changes in EIS (positive correlation) and SST (negative correlation). Kawai et al. (2017) derived the
418 linear combination from the index ECTEI and showed that a decrease in LCC under increased EIS in warmer climates can be
419 explained based on the ECTEI change (see Kawai et al. (2017) for more detail). It is true that a usage of empirical
420 relationships obtained in the present climate for climate change simulations has a possibility of causing spurious climate
421 feedback. On the other hand, we would like to note that ECTEI is even more physics-based index than EIS, the relationship
422 is not used directly for cloud formation but used as a threshold for cloud top mixing, and ECTEI can explain positive low
423 cloud feedback, although the risk of spurious climate feedback still cannot be eliminated.

424

425 4.2 Ice sedimentation and ice conversion to snow

426 4.2.1 Old treatment and problems

427 Treatment of ice sedimentation in climate models is awkward because the product of the terminal velocity of cloud ice
428 v_{ice} (typical value ~ 0.5 m s^{-1}) and the time step Δt (for example, 1800 s in MRI-CGCM3 and MRI-ESM2) can exceed the
429 thickness of the vertical layer Δz (~ 500 m) in climate models. In such cases the explicit calculation is invalid and numerical
430 instability may occur because a vertical Courant–Friedrichs–Lewy (CFL) condition is violated. To avoid this problem,
431 various measures have been taken. Rotstayn (1997) reviewed the following four treatments: (A) to set an artificial limit to
432 the sedimentation flux for preventing defective calculation; (B) to adopt a 'fall-through' assumption; (C) to use an implicit
433 scheme; and (D) to use an analytically integrated scheme. Discussing the problems associated with each treatment, he
434 concluded that the last one (D) was the most suitable. Although adopting shorter time steps for selected processes that is
435 called substepping (e.g., Morrison and Gettelman, 2008) would be an ideal solution, it can increase computational cost to
436 some degree.

437 In MRI-CGCM3, IWC was divided into ice crystals and snow using a size threshold of 100 μm. The size distribution of
438 ice particles is assumed to follow a Marshall–Palmer distribution as described in Rotstayn (1997):

439 $$P_i(D_i) = \lambda_i e^{-\lambda_i D_i}$$

440 where D_i (m) is the diameter of ice particles, λ_i (m^{-1}) is the slope factor, and the distribution $P_i(D_i)$ is normalized to 1. The
441 slope factor can be written as follows:

$$\lambda_i = \left(\frac{\pi \rho_i N_i}{\rho_a q_i}\right)^{1/3}$$

where ρ_i (kg m^{-3}) is the density of ice, N_i (m^{-3}) is the number concentration of ice crystals, ρ_a (kg m^{-3}) is air density, and q_i (kg kg^{-1}) is IWC. The ratios of cloud ice crystals with size less than 100 μm with respect to total ice crystals can be obtained analytically by integrating the probability density function as follows:

$$r_{iw} = 1 - \frac{1}{6}\{(\lambda_i D_{100})^3 + 3(\lambda_i D_{100})^2 + 6(\lambda_i D_{100}) + 6\}e^{-\lambda_i D_{100}}$$

$$r_{in} = 1 - e^{-\lambda_i D_{100}}$$

where D_{100} (m) is particle size of 1×10^{-4} (m) (= 100 μm), and r_{iw} and r_{in} are ratios of cloud ice crystals for mass and number concentrations. A sedimentation velocity (m s^{-1}) is calculated based on Heymsfield (1977), Heymsfield and Donner (1990), and Rotstayn (1997):

$$v_{ice} = 3.23 \left(\frac{\rho_a q_i r_{iw}}{a}\right)^{0.17} \tag{1}$$

where a is cloud fraction. Ice crystals of $r_{iw} q_i$ fall with sedimentation velocity v_{ice}, and snow mass $(1 - r_{iw}) q_i$ is assumed to fall down to the surface within a time step. Removal of the snow part based on this kind of diagnostic partition is used in some cloud schemes. In version CY25r1 of the ECMWF IFS (ECMWF, 2002), IWC is divided into two categories with sizes larger and smaller than 100 μm following a function in McFarquhar and Heymsfield (1997; hereafter, MH97) and the larger size portion of IWC is considered to fall through to the ground within a time step. In MRI-CGCM3, the equation of IWC to be solved is as follows:

$$\frac{\partial q_i}{\partial t} = C_g + \frac{R_i}{\rho_a \Delta z} - \frac{v_{ice}}{\Delta z} r_{iw} q_i - \frac{(1-r_{iw})q_i}{\Delta t} \tag{2}$$

where C_g (kg kg^{-1} s^{-1}) is the generation rate of IWC, R_i (kg m^{-2} s^{-1}) is the ice sedimentation flux into the layer from above, Δz (m) is the layer thickness, and Δt (s) is the model time step. The second and the third terms on the right-hand side correspond to the ice sedimentation calculation (e.g., Smith, 1990; Rotstayn, 1997). An analytically integrated solution (Rotstayn, 1997; ECMWF, 2002) was used to obtain IWC after one time step.

However, this treatment contains some problems. The first is that a part of cloud ice larger than 100 μm is eliminated from the atmosphere repeatedly when a short time step is used, because the shape of the size distribution and the ratio of ice portions larger than and smaller than 100 μm is insensitive to IWC change. This causes strong time-step dependency of IWC: IWC monotonically decreases with shorter time steps from 3600 s to 300 s as seen in Fig. 10. The second problem is that the sedimentation velocity calculated from Eq. (1) is too large for ice with size smaller than 100 μm. This is because the sedimentation velocity is supposed to represent a weighted value for the whole ice content that includes all sizes of ice, and sedimentation velocity varies widely with particle size.

4.2.2 New scheme and improvements

Considering the wide range of sedimentation velocity, the velocities of falling cloud ice representing both small and large particles are derived separately (originally reported in a preliminary report, Kawai, 2005). Observed size-distribution functions of cloud ice of MH97 and size–velocity relationships for cloud ice (Heymsfield and Iaquinta 2000) were integrated over size using a procedure similar to Zurovac-Jevtić and Zhang (2003). See Supplement A for the detailed derivation. While they derived only one velocity representing the total cloud ice, two velocities are derived in this study for a more sophisticated treatment of sedimentation. The ice-fall velocity for particles smaller [larger] than 100 μm, v_i [v_s] (m s^{-1}), is obtained as a function of ice water content smaller [larger] than 100 μm, IWC$_{<100}$ [IWC$_{>100}$] (kg m^{-3}), as below (note that the unit is not (kg kg^{-1}) but (kg m^{-3})):

$$v_i = 1.56(\text{IWC}_{<100})^{0.24} \tag{3}$$

$$v_s = 2.23(\text{IWC}_{>100})^{0.074} \tag{4}$$

Figure 14 shows the velocities v_i and v_s. The velocity of cloud ice smaller than 100 μm is much smaller than the conventionally used velocity of ice of Rotstayn (1997). Therefore, it is inappropriate to represent the velocity of ice with size smaller than 100 μm using the velocity of Eq. (1), and Eq. (3) is more appropriate for calculating the velocity. The figure also shows that cloud ice larger than 100 μm has a velocity of about 1 m s^{-1}. Therefore, the sedimentation cannot be calculated appropriately with the time step used in our climate models, and the treatment of instant fall of snow (large ice) through to the surface is unavoidable, unless substepping is introduced.

In MRI-CGCM3, it was assumed that the ratio of snow calculated from the Marshall−Palmer distribution can be applied anytime and anywhere without taking account of the history of the cloud processes. In this case, conversion of ice crystal into snow is not proportional to model time step and it causes the strong time-step dependency of IWC. If a conversion rate of ice crystals into snow is available, we can avoid this time-step dependency. To obtain the rate, we assume that the ratio given by MH97 may be regarded as a ratio between ice crystals and accumulated snow from the layers above, which is converted from ice crystals at a certain rate. In this concept, the ratio of snow should increase as the depth from the cloud top increases. In the derivation of the rate C_{I2S} (kg kg^{-1} s^{-1}), simple assumptions were introduced: (a) the concentration of cloud ice is vertically homogeneous, (b) produced snow concentration is accumulated downward, (c) the observation depth of the ratio is H_c (m) from the top of a cloud. Under these assumptions, the rate can be obtained as follows (see Appendix A for the derivation):

$$C_{I2S} = \frac{1-\alpha_i}{\alpha_i}\frac{v_s}{H_c}q_i \tag{5}$$

where α_i is the ratio of cloud ice content with particle sizes smaller than 100 μm to the total cloud ice content (see Supplement A.2 for details: Fig. S2 shows α_i and the equation is Eq. (S10)). In this study, H_c =2,000 m is assumed in reference to MH97. The equation of IWC to be solved is as follows:

$$\frac{\partial q_i}{\partial t} = C_g + \frac{R_i}{\rho_a \Delta z} - \frac{v_i}{\Delta z}q_i - D_{I2S}q_i \tag{6}$$

502 where $D_{I2s} = C_{I2s}/q_i$. Note that although the ratio α_i obtained from Eq. (S10) is used to calculate the conversion rate C_{I2s}, it is

503 not used to directly determine the ratio between small ice crystals and snow differently from in Eq. (2). An analytically

504 integrated solution is used to obtain IWC after one time step.

505   Figure 10 shows that IWC is not affected by time step in the control simulation that uses the modified scheme of ice

506 sedimentation and ice conversion to snow, while the old scheme that was used in MRI-CGCM3 shows strong time-step

507 dependency. The improvement can mainly be attributed to the fact that the conversion of ice to snow is proportional to the

508 time step: the last term of the right-hand side in Eq. (6) does not explicitly depend on $\mathit{\Delta}t$, while the one in Eq. (2) does. In

509 addition, the slower sedimentation velocity in the new formulation contributes to more reasonable calculation of ice crystal

510 sedimentation because processes with short time-scales compared to the model time step may be unphysically calculated. In

511 many climate models, the terminal velocity of cloud ice has been represented by a single velocity whose typical value is ~0.5

512 m s^{-1} (e.g., Heymsfield, 1977; Heymsfield and Donner, 1990), and the whole cloud ice content in the grid box falls with that

513 velocity (e.g., Rotstayn, 1997; Smith, 1990). However, as is evident from Fig. 14, the velocity of ice crystals smaller than

514 100 μm is ~0.1 m s^{-1} and much smaller than the typical value representing all sizes (~1 m s^{-1}). Small size ice crystals should

515 remain in the air for longer. On the other hand, some models diagnose the removal of snow portion from the total IWC

516 assuming a fixed size distribution without taking the history of the cloud processes into account (e.g., ECMWF, 2002).

517 However, this causes time-step dependency, as discussed above. Note also that size distribution must change depending on

518 the distance from the cloud top, although such dependence is not taken into account explicitly in most studies or treatments

519 in climate models. We have clarified such problems and proposed a practical solution for them in the present paper.

520

521

5 Summary

523   In the development of the climate model MRI-ESM2 that is planned for use in CMIP6 and CFMIP-3 simulations, the

524 representations of clouds are significantly improved from the previous version MRI-CGCM3 used in CMIP5 and CFMIP-2

525 simulations. The score of the spatial pattern of radiative fluxes at the top of the atmosphere for MRI-ESM2 is better than any

526 of the 48 CMIP5 models. In this paper, we presented comprehensively various modifications related to clouds, which

527 contribute to the improved cloud representation, and their main impacts. The modifications cover various schemes and

528 processes including the cloud scheme, turbulence scheme, cloud microphysics processes, the interaction between cloud and

529 convection schemes, resolution issues, cloud radiation processes, the aerosol properties, and numerics. Note that the

530 improvement of performance in climate models due to an update is ordinarily contributed by the cumulative effect of many

531 minor modifications rather than by the introduction of a new advanced scheme. In addition, the new stratocumulus

532 parameterization and improved cloud ice fall scheme are described in detail, because they include scientifically new concepts

and technically important issues. As a result, this paper will be useful for model developers and users of our CMIP6 outputs, especially those related to clouds.

The most remarkable improvement addressed the serious lack of upward shortwave radiative flux over the Southern Ocean in the old version. This improvement was obtained mainly by (i) an increase in low cloud cover due to the implementation of the new stratocumulus scheme, a new treatment of the suppression of shallow convection under stratocumulus conditions, and increased horizontal resolution for the radiation calculation, (ii) an increase in the ratio of super-cooled liquid water due to the modified treatment of the WBF effect, and (iii) an increase in cloud droplet number concentration by taking the effect of small size sea-salt aerosols into account. Items (ii) and (iii) contribute to an increase in the optical thickness of clouds. The excessive reflection of solar radiation over the tropics in MRI-CGCM3 was substantially reduced by the introduction of a new cloud overlap scheme, PICA. Increased vertical resolution from L48 to L80 and a treatment of the suppression of shallow convection under stratocumulus conditions contribute to improve the vertical structure of the transition from subtropical stratocumulus to cumulus. In addition, improved treatments of cloud ice sedimentation and conversion of cloud ice to snow, which are based on more accurate physics than the old ones, alleviated the strong time-step dependency of IWC.

However, the modifications in MRI-ESM2 are still relatively simple and ad hoc in some cases. Therefore, we should continue to develop various schemes and processes related to clouds, especially cloud microphysics and the treatment of cloud inhomogeneity within a model grid box, by introducing more sophisticated concepts.

On a final note, we acknowledge the many evaluation and intercomparison studies related to clouds for CMIP multi-models, which have given us useful information for model development (e.g., Jiang et al. (2012) for vertical profiles of cloud water content and water vapour; Lauer and Hamilton (2013) for liquid water path; Su et al. (2013) for vertical profiles of cloud fraction and cloud water content under different large-scale environments; McCoy et al. (2015) and Cesana et al. (2015) for ratios of super-cooled liquid water and ice; Nam et al. (2012) for cloud radiative effect and vertical structure of low clouds; Nuijens et al. (2015) for vertical structures and temporal variations of trade-wind cumulus; Bodas-Salcedo et al. (2014) for cloud and radiation biases over the Southern Ocean; Kawai et al. (2018) for marine fog; Suzuki et al. (2015) for warm rain formation process; Tsushima et al. (2013) for occurrence frequency and cloud radiative effect of each cloud regime). It is impossible for a modeller to examine all of these characteristics in their own model, because there are many aspects to examine even for cloud related values alone and these evaluations need specific knowledge and careful treatment. Therefore, these evaluation activities are very helpful for modellers to improve and develop their models.

Code and Data availability

Access to the simulation data can be granted upon request. The MRI-ESM2 code is the property of MRI/JMA and not available to the general public. Access to the code can be granted upon request, under a collaborative framework between MRI and related institutes or universities. The code can be provided to the editor and the reviewers for the purpose of the review of the manuscript.

Appendix

A. Derivation of the conversion rate of cloud ice crystals to snow

The conversion rate of cloud ice crystals to snow (cloud ice particles whose size is larger than 100 μm are called "snow" here) in the new treatment is derived under the simple assumptions described below. Although these assumptions are rather rough, the advantage is that this rate utilized in the scheme is derived from observational relationships for tropical cirrus.

It is assumed that the ratio between cloud ice crystals and snow is not the same throughout a cloud, but depends on the depth from the cloud top. It is presumed that the ratio of small cloud ice crystals is large near the cloud top and the ratio of snow (large cloud ice) increases downward in the cloud, because upper cloud ice crystals are continuously converted to snow and the density of snow, which falls with velocity much faster than cloud ice crystals, is accumulated downward. Therefore, the ratios should be a function of the distance from the cloud top, and the ratios α_i in MH97 should be regarded as the ratio at a certain distance from the cloud top.

To derive the conversion rate in this study, cloud ice content q_i (kg kg^{-1}) was assumed to be vertically homogeneous in the cloud. The snow density (kg m^{-3}) that is produced by a unit volume of cloud ice crystals existing at upper altitude is C_{I2S} $\rho_a v_s^{-1}$, using a conversion rate of cloud ice to snow C_{I2S} (kg kg^{-1} s^{-1}). Consequently, the snow density at height z can be written as follows, using the cloud top height z_{ctop}.

$$\int_z^{z_{ctop}} C_{I2S} \frac{\rho_a}{v_s} dz \approx \frac{z_{ctop} - z}{v_s} \rho_a C_{I2S}$$

where a constant value is used for ρ_a regardless of the height for simplicity. Then snow content per unit air mass is $C_{I2S} H_c$ v_s^{-1} (kg kg^{-1}) using $H_c \equiv z_{ctop} - z$. On the other hand, the ratio of cloud ice crystals to snow can be written as follows using the observational function α_i by MH97:

$$q_i : \frac{H_c}{v_s} C_{I2S} = \alpha_i : 1 - \alpha_i$$

Therefore, C_{I2S} can be derived as follows:

$$C_{I2S} = \frac{1 - \alpha_i}{\alpha_i} \frac{v_s}{H_c} q_i$$

Author contribution

HK was responsible for most aspects of model developments related to the representation of clouds. SY performed tuning of clouds simulated in MRI-ESM2 and many sensitivity tests. TK performed coding related to aerosol optical properties and the output format of the model. NO and TT developed the aerosol model and contributed to the improvements of the aerosol radiation and aerosol cloud interactions. RN developed PICA and HY implemented the scheme into MRI-ESM2. SY and TK performed many model simulations, and TK and HY contributed to find coding problems in the original cloud scheme. All authors contributed to related discussions. HK wrote the first draft of the article, and all authors contributed to the writing of the final version of the article.

Acknowledgements

We acknowledge the editor for handling this paper and the two anonymous reviewers for their supportive and insightful comments. Several datasets (Pincus et al., 2012; Zhang et al., 2012) used in this work were obtained from the obs4MIPs project (https://www.earthsystemcog.org/projects/obs4mips/) hosted on the Earth System Grid Federation (http://esgf.llnl.gov). This study was partly supported by "Integrated Research Program for Advancing Climate Models: TOUGOU" from the Ministry of Education, Culture, Sports, Science and Technology (MEXT), Japan. Additionally, it was supported by the Japan Society for the Promotion of Science (JSPS) KAKENHI Grant Numbers JP26701004, JP16H01772, JP18H05292, JP18H03363, and JP19K03977 and the Environment Research and Technology Development Fund (2-1703 and S-12) of the Environmental Restoration and Conservation Agency, Japan. Kohei Yoshida made efforts to determine vertical model levels in MRI-ESM2, and Eiki Shindo kindly supported HK to perform model experiments.

References

Abdul-Razzak, H. and Ghan, S. J.: A parameterization of aerosol activation: 2. Multiple aerosol types, J. Geophys. Res., 105(D5), 6837, doi:10.1029/1999JD901161, 2000.

Abdul-Razzak, H., Ghan, S. J. and Rivera-Carpio, C.: A parameterization of aerosol activation: 1. Single aerosol type, J. Geophys. Res., 103(D6), 6123, doi:10.1029/97JD03735, 1998.

Abel, S. J., Walters, D. N. and Allen, G.: Evaluation of stratocumulus cloud prediction in the Met Office forecast model during VOCALS-REx, Atmos. Chem. Phys., 10(21), 10541–10559, doi:10.5194/acp-10-10541-2010, 2010.

Betts, A. K.: Diurnal variation of California coastal stratocumulus from two days of boundary layer soundings, Tellus A, 42(2), 302–304, doi:10.1034/j.1600-0870.1990.t01-1-00007.x, 1990.

Betts, A. K. and Boers, R.: A Cloudiness Transition in a Marine Boundary Layer, J. Atmos. Sci., 47(12), 1480–1497, doi:10.1175/1520-0469(1990)047<1480:ACTIAM>2.0.CO;2, 1990.

Bigg, E. K.: The supercooling of water, Proc. Phys. Soc., B66, London, 688-694, 1953.

Bodas-Salcedo, A., Williams, K. D., Ringer, M. A., Beau, I., Cole, J. N. S., Dufresne, J. L., Koshiro, T., Stevens, B., Wang, Z. and Yokohata, T.: Origins of the solar radiation biases over the Southern Ocean in CFMIP2 models, J. Clim., 27(1), 41–56, doi:10.1175/JCLI-D-13-00169.1, 2014.

Bodas-Salcedo, A., Hill, P. G., Furtado, K., Williams, K. D., Field, P. R., Manners, J. C., Hyder, P. and Kato, S.: Large contribution of supercooled liquid clouds to the solar radiation budget of the Southern Ocean, J. Clim., 29(11), 4213–4228, doi:10.1175/JCLI-D-15-0564.1, 2016.

Bony, S., Webb, M., Bretherton, C., Klein, S., Siebesma, P., Tselioudis, G. and Zhang, M.: CFMIP: Towards a better evaluation and understanding of clouds and cloud feedbacks in CMIP5 models, Clivar Exch, 56(2008), 2, 2011.

Bretherton, C. S., Wood, R., George, R. C., Leon, D., Allen, G. and Zheng, X.: Southeast Pacific stratocumulus clouds, precipitation and boundary layer structure sampled along 20° S during VOCALS-REx, Atmos. Chem. Phys., 10(21), 10639–10654, doi:10.5194/acp-10-10639-2010, 2010.

Brooks, M. E., Hogan, R. J. and Illingworth, A. J.: Parameterizing the Difference in Cloud Fraction Defined by Area and by Volume as Observed with Radar and Lidar, J. Atmos. Sci., 62(7), 2248–2260, doi:10.1175/JAS3467.1, 2005.

Bushell, A. C. and Martin, G. M.: The impact of vertical resolution upon GCM simulations of marine stratocumulus, Clim. Dyn., 15(4), 293–318, doi:10.1007/s003820050283, 1999.

Caldwell, P. and Bretherton, C. S.: Response of a Subtropical Stratocumulus-Capped Mixed Layer to Climate and Aerosol Changes, J. Clim., 22(1), 20–38, doi:10.1175/2008JCLI1967.1, 2009.

Caldwell, P. M., Zhang, Y. and Klein, S. A.: CMIP3 subtropical stratocumulus cloud feedback interpreted through a mixed-layer model, J. Clim., 26(5), 1607–1625, doi:10.1175/JCLI-D-12-00188.1, 2013.

Cesana, G. and Chepfer, H.: Evaluation of the cloud thermodynamic phase in a climate model using CALIPSO-GOCCP, J. Geophys. Res. Atmos., 118(14), 7922–7937, doi:10.1002/jgrd.50376, 2013.

Cesana, G., Waliser, D. E., Jiang, X. and Li, J. L. F.: Multimodel evaluation of cloud phase transition using satellite and reanalysis data, J. Geophys. Res. Atmos., 120(15), 7871–7892, doi:10.1002/2014JD022932, 2015.

Cesana, G., Chepfer, H., Winker, D., Getzewich, B., Cai, X., Jourdan, O., Mioche, G., Okamoto, H., Hagihara, Y., Noel, V. and Reverdy, M.: Using in situ airborne measurements to evaluate three cloud phase products derived from CALIPSO, J. Geophys. Res. Atmos., 121(10), 5788–5808, doi:10.1002/2015JD024334, 2016.

Chin, M., Ginoux, P., Kinne, S., Torres, O., Holben, B. N., Duncan, B. N., Martin, R. V., Logan, J. a., Higurashi, A. and Nakajima, T.: Tropospheric Aerosol Optical Thickness from the GOCART Model and Comparisons with Satellite and Sun Photometer Measurements, J. Atmos. Sci., 59(3), 461–483, doi:10.1175/1520-0469(2002)059<0461:TAOTFT>2.0.CO;2, 2002.

Clarke, A. D., Owens, S. R. and Zhou, J.: An ultrafine sea-salt flux from breaking waves: Implications for cloud condensation nuclei in the remote marine atmosphere, J. Geophys. Res. Atmos., 111(6), 1–14, doi:10.1029/2005JD006565, 2006.

Collins, W. D.: Parameterization of Generalized Cloud Overlap for Radiative Calculations in General Circulation Models, J. Atmos. Sci., 58(21), 3224–3242, doi:10.1175/1520-0469(2001)058<3224:POGCOF>2.0.CO;2, 2001.

Cotton, W. R., Tripoli, G. J., Rauber, R. M. and Mulvihill, E. a.: Numerical Simulation of the Effects of Varying Ice Crystal Nucleation Rates and Aggregation Processes on Orographic Snowfall, J. Clim. Appl. Meteorol., 25(11), 1658–1680, doi:10.1175/1520-0450(1986)025<1658:NSOTEO>2.0.CO;2, 1986.

Covert, D. S., Kapustin, V. N., Bates, T. S. and Quinn, P. K.: Physical properties of marine boundary layer aerosol particles of the mid-Pacific in relation to sources and meteorological transport, J. Geophys. Res. Atmos., 101(D3), 6919–6930, doi:10.1029/95JD03068, 1996.

Deardorff, J. W.: Cloud Top Entrainment Instability, J. Atmos. Sci., 37(1), 131–147, doi:10.1175/1520-0469(1980)037<0131:CTEI>2.0.CO;2, 1980.

Duynkerke, P. G. and Teixeira, J.: Comparison of the ECMWF Reanalysis with FIRE I Observations: Diurnal Variation of Marine Stratocumulus, J. Clim., 14(7), 1466–1478, doi:10.1175/1520-0442(2001)014<1466:COTERW>2.0.CO;2, 2001.

ECMWF: Clouds and large-scale precipitation, IFS Documentation, European Centre for Medium-Range Weather Forecasts, CY25r1, Part IV, Chapter 6, 2002.

ECMWF: Clouds and large-scale precipitation, IFS Documentation, European Centre for Medium-Range Weather Forecasts, CY43r3, Part IV, Chapter 7, 2017.

Eyring, V., Bony, S., Meehl, G. A., Senior, C., Stevens, B., Stouffer, R. J. and Taylor, K. E.: Overview of the Coupled Model Intercomparison Project Phase 6 (CMIP6) experimental design and organisation, Geosci. Model Dev. Discuss., 8(12), 10539–10583, doi:10.5194/gmdd-8-10539-2015, 2015.

Forbes, R. M. and Ahlgrimm, M.: On the Representation of High-Latitude Boundary Layer Mixed-Phase Cloud in the ECMWF Global Model, Mon. Weather Rev., 142(9), 3425–3445, doi:10.1175/MWR-D-13-00325.1, 2014.

Forbes, R. M., Geer, A., Lonitz, K., and Ahlgrimm, M.: Reducing systematic errors in cold-air outbreaks, ECMWF Newsletter, No. 146, European Centre for Medium-Range Weather Forecasts, 17–22, https://doi.org/10.21957/s41h7q7l, 2016.

Frey, W. R. and Kay, J. E.: The influence of extratropical cloud phase and amount feedbacks on climate sensitivity, Clim. Dyn., 50(7–8), 3097–3116, doi:10.1007/s00382-017-3796-5, 2018.

Geleyn, J.-F., and Hollingsworth, A.: An economical analytical method for the computation of the interaction between scattering and line absorption of radiation, Beitr. Phys. Atmos., 52, 1-16, 1979.

Guo, Z., Wang, M., Qian, Y., Larson, V. E., Ghan, S., Ovchinnikov, M., Bogenschutz, P. A., Zhao, C., Lin, G. and Zhou, T.: A sensitivity analysis of cloud properties to CLUBB parameters in the single-column Community Atmosphere Model (SCAM5), J. Adv. Model. Earth Syst., 6(3), 829–858, doi:10.1002/2014MS000315, 2015.

Hahn, C. J., and Warren, S. G.: Extended edited synoptic cloud reports from ships and land stations over the globe, 1952–1996 (2009 update). NDP-026C, Carbon Dioxide Information Analysis Center, Oak Ridge National Laboratory, Oak Ridge, TN, 2009.

Heymsfield, A. J.: Precipitation Development in Stratiform Ice Clouds: A Microphysical and Dynamical Study, J. Atmos. Sci., 34(2), 367–381, doi:10.1175/1520-0469(1977)034<0367:PDISIC>2.0.CO;2, 1977.

Heymsfield, A. J. and Donner, L. J.: A Scheme for Parameterizing Ice-Cloud Water Content in General Circulation Models, J. Atmos. Sci., 47(15), 1865–1877, doi:10.1175/1520-0469(1990)047<1865:ASFPIC>2.0.CO;2, 1990.

Heymsfield, A. J. and Iaquinta, J.: Cirrus Crystal Terminal Velocities, J. Atmos. Sci., 57(7), 916–938, doi:10.1175/1520-0469(2000)057<0916:CCTV>2.0.CO;2, 2000.

Hoose, C., Kristjánsson, J. E., Iversen, T., Kirkevåg, A., Seland, Ø. and Gettelman, A.: Constraining cloud droplet number concentration in GCMs suppresses the aerosol indirect effect, Geophys. Res. Lett., 36(12), L12807, doi:10.1029/2009GL038568, 2009.

Hu, Y., Rodier, S., Xu, K. M., Sun, W., Huang, J., Lin, B., Zhai, P. and Josset, D.: Occurrence, liquid water content, and fraction of supercooled water clouds from combined CALIOP/IIR/MODIS measurements, J. Geophys. Res. Atmos., 115(19), 1–13, doi:10.1029/2009JD012384, 2010.

Jakob, C.: The representation of cloud cover in Atmospheric General Circulation Models, A thesis submitted to the Fakultat fur Physik der Ludwig-Maximilians-Universitat, European Centre for Medium-Range Weather Forecasts, 2000.

Jiang, J. H., Su, H., Zhai, C., Perun, V. S., Del Genio, A., Nazarenko, L. S., Donner, L. J., Horowitz, L., Seman, C., Cole, J., Gettelman, A., Ringer, M. a., Rotstayn, L., Jeffrey, S., Wu, T., Brient, F., Dufresne, J. L., Kawai, H., Koshiro, T., Watanabe, M., Lécuyer, T. S., Volodin, E. M., Iversen, T., Drange, H., Mesquita, M. D. S., Read, W. G., Waters, J. W., Tian, B., Teixeira, J. and Stephens, G. L.: Evaluation of cloud and water vapor simulations in CMIP5 climate models Using NASA "A-Train" satellite observations, J. Geophys. Res. Atmos., 117(14), doi:10.1029/2011JD017237, 2012.

Jones, A., Roberts, D. L., Woodage, M. J. and Johnson, C. E.: Indirect sulphate aerosol forcing in a climate model with an interactive sulphur cycle, J. Geophys. Res. Atmos., 106(D17), 20293–20310, doi:10.1029/2000JD000089, 2001.

Kärcher, B. and Lohmann, U.: A Parameterization of cirrus cloud formation: Homogeneous freezing including effects of aerosol size, J. Geophys. Res. Atmos., 107(D23), AAC 9-1-AAC 9-10, doi:10.1029/2001JD001429, 2002.

Kärcher, B., and Lohmann, U.: A parameterization of cirrus cloud formation: Heterogeneous freezing, J. Geophys. Res., 108, D14, 4402, https://doi.org/10.1029/2002JD003220, 2003.

Kärcher, B., Hendricks, J. and Lohmann, U.: Physically based parameterization of cirrus cloud formation for use in global atmospheric models, J. Geophys. Res., 111(D1), 1–11, doi:10.1029/2005JD006219, 2006.

Kawai, H.: Improvement of a Cloud Ice Fall Scheme in GCM, CAS/JSC WGNE Research Activities in Atmospheric and Oceanic Modelling/WMO, 35, 4.11-4.12, 2005.

Kawai, H.: Improvement of a Stratocumulus Scheme for Mid-latitude Marine Low Clouds, CAS/JSC WGNE Research Activities in Atmospheric and Oceanic Modelling/WMO, 43, 4.03-4.04, 2013.

Kawai, H. and Inoue, T.: A simple parameterization scheme for subtropical marine stratocumulus, Sci. Online Lett. Atmos., 2, doi:10.2151/sola.2006-005, 2006.

Kawai, H., Yabu, S., Hagihara, Y., Koshiro, T. and Okamoto, H.: Characteristics of the cloud top heights of marine boundary layer clouds and the frequency of marine fog over mid-latitudes, J. Meteorol. Soc. Japan, 93(6), doi:10.2151/jmsj.2015-045, 2015.

Kawai, H., Koshiro, T., Webb, M., Yukimoto, S., and Tanaka, T.: Cloud feedbacks in MRI-CGCM3, CAS/JSC WGNE Research Activities in Atmospheric and Oceanic Modelling/WMO, 45, 7.11-7.12, 2015.

Kawai, H., Koshiro, T. and Webb, M. J.: Interpretation of factors controlling low cloud cover and low cloud feedback using a unified predictive index, J. Clim., 30(22), doi:10.1175/JCLI-D-16-0825.1, 2017.

Kawai, H., Koshiro, T., Endo, H. and Arakawa, O.: Changes in marine fog over the North Pacific under different climates in CMIP5 multimodel simulations, J. Geophys. Res. Atmos., 123(19), 10911–10924, doi:10.1029/2018JD028899, 2018.

Kay, J. E., Wall, C., Yettella, V., Medeiros, B., Hannay, C., Caldwell, P. and Bitz, C.: Global climate impacts of fixing the Southern Ocean shortwave radiation bias in the Community Earth System Model (CESM), J. Clim., 0–53, doi:10.1017/CBO9781107415324.004, 2016.

Klein, S. A. and Hartmann, D. L.: The seasonal cycle of low stratiform clouds, J. Clim., 6(8), 1587–1606, doi:10.1175/1520-0442(1993)006<1587:TSCOLS>2.0.CO;2, 1993.

Koshiro, T., Shiotani, M., Kawai, H. and Yukimoto, S.: Evaluation of Relationships between Subtropical Marine Low Stratiform Cloudiness and Estimated Inversion Strength in CMIP5 Models Using the Satellite Simulator Package COSP, SOLA, 14(0), 25–32, doi:10.2151/sola.2018-005, 2018.

Kuo, H.-C. and Schubert, W. H.: Stability of cloud-topped boundary layers, Q. J. R. Meteorol. Soc., 114(482), 887–916, doi:10.1002/qj.49711448204, 1988.

Larson, K., Hartmann, D. L. and Klein, S. a.: The Role of Clouds, Water Vapor, Circulation, and Boundary Layer Structure in the Sensitivity of the Tropical Climate, J. Clim., 12(8), 2359–2374, doi:10.1175/1520-0442(1999)012<2359:TROCWV>2.0.CO;2, 1999.

Lauer, A. and Hamilton, K.: Simulating Clouds with Global Climate Models: A Comparison of CMIP5 Results with CMIP3 and Satellite Data, J. Clim., 26(11), 3823–3845, doi:10.1175/JCLI-D-12-00451.1, 2013.

Lauer, A., Hamilton, K., Wang, Y., Phillips, V. T. J. and Bennartz, R.: The Impact of Global Warming on Marine Boundary Layer Clouds over the Eastern Pacific—A Regional Model Study, J. Clim., 23(21), 5844–5863, doi:10.1175/2010JCLI3666.1, 2010.

755 Levkov, L., Rockel, B., Kapitza, H., and Raschke, E.: 3D mesoscale numerical studies of cirrus and stratus clouds by their
756   time and space evolution, Beitr. Phys. Atmos., 65, 35–58, 1992.

757 Li, J. L. F., Waliser, D. E., Stephens, G., Lee, S., L'Ecuyer, T., Kato, S., Loeb, N. and Ma, H. Y.: Characterizing and
758   understanding radiation budget biases in CMIP3/CMIP5 GCMs, contemporary GCM, and reanalysis, J. Geophys. Res.
759   Atmos., 118(15), 8166–8184, doi:10.1002/jgrd.50378, 2013.

760 Liu, X., Easter, R. C., Ghan, S. J., Zaveri, R., Rasch, P., Shi, X., Lamarque, J. F., Gettelman, A., Morrison, H., Vitt, F.,
761   Conley, A., Park, S., Neale, R., Hannay, C., Ekman, A. M. L., Hess, P., Mahowald, N., Collins, W., Iacono, M. J.,
762   Bretherton, C. S., Flanner, M. G. and Mitchell, D.: Toward a minimal representation of aerosols in climate models:
763   Description and evaluation in the Community Atmosphere Model CAM5, Geosci. Model Dev., 5(3), 709–739,
764   doi:10.5194/gmd-5-709-2012, 2012.

765 Lock, A. P.: Factors influencing cloud area at the capping inversion for shallow cumulus clouds, Q. J. R. Meteorol. Soc.,
766   135(641), 941–952, doi:10.1002/qj.424, 2009.

767 Loeb, N. G., Wielicki, B. A., Doelling, D. R., Smith, G. L., Keyes, D. F., Kato, S., Manalo-Smith, N. and Wong, T.: Toward
768   Optimal Closure of the Earth's Top-of-Atmosphere Radiation Budget, J. Clim., 22(3), 748–766,
769   doi:10.1175/2008JCLI2637.1, 2009.

770 Lohmann, U.: Possible Aerosol Effects on Ice Clouds via Contact Nucleation, J. Atmos. Sci., 59(3), 647–656,
771   doi:10.1175/1520-0469(2001)059<0647:PAEOIC>2.0.CO;2, 2002.

772 Lohmann, U. and Diehl, K.: Sensitivity Studies of the Importance of Dust Ice Nuclei for the Indirect Aerosol Effect on
773   Stratiform Mixed-Phase Clouds, J. Atmos. Sci., 63(3), 968–982, doi:10.1175/JAS3662.1, 2006.

774 Lohmann, U., Stier, P., Hoose, C., Ferrachat, S., Kloster, S., Roeckner, E. and Zhang, J.: Cloud microphysics and aerosol
775   indirect effects in the global climate model ECHAM5-HAM, Atmos. Chem. Phys., 7(13), 3425–3446, doi:10.5194/acp-
776   7-3425-2007, 2007.

777 MacVean, M. K.: A Numerical Investigation of the Criterion for Cloud-Top Entrainment Instability, J. Atmos. Sci., 50(15),
778   2481–2495, doi:10.1175/1520-0469(1993)050<2481:ANIOTC>2.0.CO;2, 1993.

779 MacVean, M. K. and Mason, P. J.: Cloud-Top Entrainment Instability through Small-Scale Mixing and Its Parameterization
780   in Numerical Models, J. Atmos. Sci., 47(8), 1012–1030, doi:10.1175/1520-0469(1990)047<1012:CTEITS>2.0.CO;2,
781   1990.

782 Manton, M. J., and Cotton, W. R.: Formulation of approximate equations for modeling moist deep convection on the
783   mesoscale, Atmospheric Science Paper, No. 266, Colorado State University, 1977.

784 Mauritsen, T., Stevens, B., Roeckner, E., Crueger, T., Esch, M., Giorgetta, M., Haak, H., Jungclaus, J., Klocke, D., Matei, D.,
785   Mikolajewicz, U., Notz, D., Pincus, R., Schmidt, H. and Tomassini, L.: Tuning the climate of a global model, , 4, 1–18,
786   doi:10.1029/2012MS000154, 2012.

787 McCoy, D. T., Hartmann, D. L., Zelinka, M. D., Ceppi, P. and Grosvenor, D. P.: Mixed-phase cloud physics and Southern
788   Ocean cloud feedback in climate models, J. Geophys. Res. Atmos., 120(18), 9539–9554, doi:10.1002/2015JD023603,
789   2015.

790 McFarquhar, G. M. and Heymsfield, A. J.: Parameterization of Tropical Cirrus Ice Crystal Size Distributions and
791   Implications for Radiative Transfer: Results from CEPEX, J. Atmos. Sci., 54(17), 2187–2200, doi:10.1175/1520-
792   0469(1997)054<2187:POTCIC>2.0.CO;2, 1997.

793 Medeiros, B., Stevens, B., Held, I. M., Zhao, M., Williamson, D. L., Olson, J. G. and Bretherton, C. S.: Aquaplanets,
794   Climate Sensitivity, and Low Clouds, J. Clim., 21(19), 4974–4991, doi:10.1175/2008JCLI1995.1, 2008.

795 Meyers, M. P., DeMott, P. J. and Cotton, W. R.: New Primary Ice-Nucleation Parameterizations in an Explicit Cloud Model,
796   J. Appl. Meteorol., 31(7), 708–721, doi:10.1175/1520-0450(1992)031<0708:NPINPI>2.0.CO;2, 1992.

797 Miller, R. L.: Tropical Thermostats and Low Cloud Cover, J. Clim., 10(3), 409–440, doi:10.1175/1520-
798   0442(1997)010<0409:TTALCC>2.0.CO;2, 1997.

799 Morrison, H. and Gettelman, A.: A New Two-Moment Bulk Stratiform Cloud Microphysics Scheme in the Community
800   Atmosphere Model, Version 3 (CAM3). Part I: Description and Numerical Tests, J. Clim., 21(15), 3642–3659,
801   doi:10.1175/2008JCLI2105.1, 2008.

802 Murakami, M.: Numerical Modeling of Dynamical and Microphysical Evolution of an Isolated Convective Cloud - The 19
803   July 1981 CCOPE cloud, J. Meteor. Soc. Japan, 68(April), 107–128, doi:10.2151/jmsj1965.68.2_107, 1990.

804 Nagasawa, R.: The Problem of Cloud Overlap in the Radiation Process of JMA's Global NWP Model, CAS/JSC WGNE
805   Research Activities in Atmospheric and Oceanic Modelling/WMO, 42, 0415-0416, 2012.

806 Nam, C., Bony, S., Dufresne, J. L. and Chepfer, H.: The too few, too bright tropical low-cloud problem in CMIP5 models,
807   Geophys. Res. Lett., 39(21), 1–7, doi:10.1029/2012GL053421, 2012.

808 Neubauer, D., Lohmann, U., Hoose, C. and Frontoso, M. G.: Impact of the representation of marine stratocumulus clouds on
809   the anthropogenic aerosol effect, Atmos. Chem. Phys., 14(21), 11997–12022, doi:10.5194/acp-14-11997-2014, 2014.

810 Nuijens, L., Medeiros, B., Sandu, I. and Ahlgrimm, M.: The behavior of trade-wind cloudiness in observations and models:
811   The major cloud components and their variability, J. Adv. Model. Earth Syst., 7(2), 600–616,
812   doi:10.1002/2014MS000390, 2015.

813 Pincus, R., Platnick, S., Ackerman, S. A., Hemler, R. S. and Patrick Hofmann, R. J.: Reconciling simulated and observed
814   views of clouds: MODIS, ISCCP, and the limits of instrument simulators, J. Clim., 25(13), 4699–4720,
815   doi:10.1175/JCLI-D-11-00267.1, 2012.

816 Qu, X., Hall, A., Klein, S. A. and Caldwell, P. M.: On the spread of changes in marine low cloud cover in climate model
817   simulations of the 21st century, Clim. Dyn., 42(9–10), 2603–2626, doi:10.1007/s00382-013-1945-z, 2014.

818 Rahn, D. A. and Garreaud, R.: Marine boundary layer over the subtropical southeast Pacific during VOCALS-REx – Part 1:
819   Mean structure and diurnal cycle, Atmos. Chem. Phys., 10(10), 4491–4506, doi:10.5194/acp-10-4491-2010, 2010.

Randall, D. A.: Conditional Instability of the First Kind Upside-Down, J. Atmos. Sci., 37(1), 125–130, doi:10.1175/1520-0469(1980)037<0125:CIOTFK>2.0.CO;2, 1980.

Rossow, W. B. and Schiffer, R. A.: Advances in Understandig Clouds from ISCCP, Bull. Am. Meteorol. Soc., 80(11), 2261–2287, doi:10.1175/1520-0477(1999)080<2261:AIUCFI>2.0.CO;2, 1999.

Rotstayn, L. D.: A physically based scheme for the treatment of stratiform clouds and precipitation in large-scale models. I: Description and evaluation of the microphysical processes, Q. J. R. Meteorol. Soc., 123(541), 1227–1282, doi:10.1002/qj.49712354106, 1997.

Rotstayn, L. D.: On the "tuning" of autoconversion parameterizations in climate models, J. Geophys. Res. Atmos., 105(D12), 15495–15507, doi:10.1029/2000JD900129, 2000.

Rutledge, S. a. and Hobbs, P.: The Mesoscale and Microscale Structure and Organization of Clouds and Precipitation in Midlatitude Cyclones. VIII: A Model for the "Seeder-Feeder" Process in Warm-Frontal Rainbands, J. Atmos. Sci., 40(5), 1185–1206, doi:10.1175/1520-0469(1983)040<1185:TMAMSA>2.0.CO;2, 1983.

Seinfeld, J. H., and Pandis, S. N.: Atmospheric Chemistry and Physics: From Air Pollution to Climate Change 2nd ed, John Wiley & Sons, New York, USA, 1203, 2006.

Siebesma, A. P., Jakob, C., Lenderink, G., Neggers, R. A. J., Teixeira, J., van Meijgaard, E., Calvo, J., Chlond, A., Grenier, H., Jones, C., Köhler, M., Kitagawa, H., Marquet, P., Lock, A. P., Müller, F., Olmeda, D. C. and Severijns, C.: Cloud representation in general-circulation models over the northern Pacific Ocean: A EUROCS intercomparison study, Q. J. R. Meteorol. Soc., 130(604), 3245–3267, doi:10.1256/qj.03.146, 2004.

Slingo, J. M.: A cloud parametrization scheme derived from GATE data for use with a numerical model, Q. J. R. Meteorol. Soc., 106(450), 747–770, doi:10.1002/qj.49710645008, 1980.

Slingo, J. M.: The Development and Verification of A Cloud Prediction Scheme For the Ecmwf Model, Q. J. R. Meteorol. Soc., 113(477), 899–927, doi:10.1002/qj.49711347710, 1987.

Smith, R. N. B.: A scheme for predicting layer clouds and their water content in a general circulation model, Q. J. R. Meteorol. Soc., 116(492), 435–460, doi:10.1002/qj.49711649210, 1990.

Soden, B. J. and Held, I. M.: An Assessment of Climate Feedbacks in Coupled Ocean – Atmosphere Models, J. Clim., 19(2003), 3354–3360, doi:10.1175/JCLI9028.1, 2006.

Soden, B. J., Held, I. M., Colman, R. C., Shell, K. M., Kiehl, J. T. and Shields, C. A.: Quantifying climate feedbacks using radiative kernels, J. Clim., 21(14), 3504–3520, doi:10.1175/2007JCLI2110.1, 2008.

Su, H., Jiang, J. H., Zhai, C., Perun, V. S., Shen, J. T., Del Genio, A., Nazarenko, L. S., Donner, L. J., Horowitz, L., Seman, C., Morcrette, C., Petch, J., Ringer, M., Cole, J., Von Salzen, K., Mesquita, M. D. S., Iversen, T., Kristjansson, J. E., Gettelman, A., Rotstayn, L., Jeffrey, S., Dufresne, J. L., Watanabe, M., Kawai, H., Koshiro, T., Wu, T., Volodin, E. M., L'Ecuyer, T., Teixeira, J. and Stephens, G. L.: Diagnosis of regime-dependent cloud simulation errors in CMIP5 models using "a-Train" satellite observations and reanalysis data, J. Geophys. Res. Atmos., 118(7), 2762–2780, doi:10.1029/2012JD018575, 2013.

854 Suzuki, K., Stephens, G., Bodas-Salcedo, A., Wang, M., Golaz, J.-C., Yokohata, T. and Koshiro, T.: Evaluation of the Warm
855   Rain Formation Process in Global Models with Satellite Observations, J. Atmos. Sci., 72(10), 3996–4014,
856   doi:10.1175/JAS-D-14-0265.1, 2015.

857 Takemura, T., Nozawa, T., Emori, S., Nakajima, T. Y. and Nakajima, T.: Simulation of climate response to aerosol direct
858   and indirect effects with aerosol transport-radiation model, J. Geophys. Res. D Atmos., 110(2), 1–16,
859   doi:10.1029/2004JD005029, 2005.

860 Tan, I. and Storelvmo, T.: Sensitivity Study on the Influence of Cloud Microphysical Parameters on Mixed-Phase Cloud
861   Thermodynamic Phase Partitioning in CAM5, J. Atmos. Sci., 73(2), 709–728, doi:10.1175/JAS-D-15-0152.1, 2016.

862 Tan, I., Storelvmo, T. and Zelinka, M. D.: Observational constraints on mixed-phase clouds imply higher climate sensitivity,
863   Science (80-.)., 352(6282), 224–227, doi:10.1126/science.aad5300, 2016.

864 Tanaka, T. Y., Orito, K., Sekiyama, T. T., Shibata, K., Chiba, M. and Tanaka, H.: MASINGAR, a global tropospheric
865   aerosol chemical transport model coupled with MRI/JMA98 GCM: Model description, Pap. Meteorol. Geophys., 53(4),
866   119–138, doi:10.2467/mripapers.53.119, 2003.

867 Taylor, K. E.: Summarizing multiple aspects of model performance in a single diagram, J. Geophys. Res. Atmos., 106(D7),
868   7183–7192, doi:10.1029/2000JD900719, 2001.

869 Taylor, K. E., Stouffer, R. J. and Meehl, G. A.: An Overview of CMIP5 and the Experiment Design, Bull. Am. Meteorol.
870   Soc., 93(4), 485–498, doi:10.1175/BAMS-D-11-00094.1, 2012.

871 Teixeira, J.: The impact of increased boundary layer vertical resolution on the ECMWF forecast system, ECMWF technical
872   memorandum, European Centre for Medium-Range Weather Forecasts, 268, 1-55, 1999.

873 Tiedtke, M.: Representation of Clouds in Large-Scale Models, Mon. Wea. Rev., 121, 3040–3061, 1993.

874 Trenberth, K. E. and Fasullo, J. T.: Simulation of present-day and twenty-first-century energy budgets of the southern oceans,
875   J. Clim., 23(2), 440–454, doi:10.1175/2009JCLI3152.1, 2010.

876 Tsushima, Y., Emori, S., Ogura, T., Kimoto, M., Webb, M. J., Williams, K. D., Ringer, M. A., Soden, B. J., Li, B. and
877   Andronova, N.: Importance of the mixed-phase cloud distribution in the control climate for assessing the response of
878   clouds to carbon dioxide increase: a multi-model study, Clim. Dyn., 27(2–3), 113–126, doi:10.1007/s00382-006-0127-
879   7, 2006.

880 Tsushima, Y., Ringer, M. A., Webb, M. J. and Williams, K. D.: Quantitative evaluation of the seasonal variations in climate
881   model cloud regimes, Clim. Dyn., 41(9–10), 2679–2696, doi:10.1007/s00382-012-1609-4, 2013.

882 Tsushima, Y., Ringer, M. A., Koshiro, T., Kawai, H., Roehrig, R., Cole, J., Watanabe, M., Yokohata, T., Bodas-Salcedo, A.,
883   Williams, K. D. and Webb, M. J.: Robustness, uncertainties, and emergent constraints in the radiative responses of
884   stratocumulus cloud regimes to future warming, Clim. Dyn., 46(9–10), doi:10.1007/s00382-015-2750-7, 2016.

885 Uppala, S. M., KÅllberg, P. W., Simmons, A. J., Andrae, U., Bechtold, V. D. C., Fiorino, M., Gibson, J. K., Haseler, J.,
886   Hernandez, A., Kelly, G. A., Li, X., Onogi, K., Saarinen, S., Sokka, N., Allan, R. P., Andersson, E., Arpe, K.,
887   Balmaseda, M. A., Beljaars, A. C. M., Berg, L. Van De, Bidlot, J., Bormann, N., Caires, S., Chevallier, F., Dethof, A.,

888   Dragosavac, M., Fisher, M., Fuentes, M., Hagemann, S., Hólm, E., Hoskins, B. J., Isaksen, L., Janssen, P. A. E. M.,
889   Jenne, R., Mcnally, A. P., Mahfouf, J.-F., Morcrette, J.-J., Rayner, N. A., Saunders, R. W., Simon, P., Sterl, A.,
890   Trenberth, K. E., Untch, A., Vasiljevic, D., Viterbo, P. and Woollen, J.: The ERA-40 re-analysis, Q. J. R. Meteorol.
891   Soc., 131(612), 2961–3012, doi:10.1256/qj.04.176, 2005.

892 Wang, Y., Xu, H. and Xie, S.-P.: Regional Model Simulations of Marine Boundary Layer Clouds over the Southeast Pacific
893   off South America. Part II: Sensitivity Experiments*, Mon. Weather Rev., 132(11), 2650–2668,
894   doi:10.1175/MWR2812.1, 2004.

895 Webb, M. J., Lambert, F. H. and Gregory, J. M.: Origins of differences in climate sensitivity, forcing and feedback in
896   climate models, Clim. Dyn., 40(3–4), 677–707, doi:10.1007/s00382-012-1336-x, 2013.

897 Webb, M. J., Andrews, T., Bodas-salcedo, A., Bony, S., Bretherton, C. S., Chadwick, R., Chepfer, H., Douville, H., Good, P.,
898   Kay, J. E., Klein, S. A., Marchand, R., Medeiros, B., Siebesma, A. P., Skinner, C. B. and Stevens, B.: The Cloud
899   Feedback Model Intercomparison Project (CFMIP) contribution to CMIP6, , (7), 359–384, doi:10.5194/gmd-10-359-
900   2017, 2017.

901 Williams, K. D., Ringer, M. A., Senior, C. A., Webb, M. J., McAvaney, B. J., Andronova, N., Bony, S., Dufresne, J. L.,
902   Emori, S., Gudgel, R., Knutson, T., Li, B., Lo, K., Musat, I., Wegner, J., Slingo, A. and Mitchell, J. F. B.: Evaluation of
903   a component of the cloud response to climate change in an intercomparison of climate models, Clim. Dyn., 26(2–3),
904   145–165, doi:10.1007/s00382-005-0067-7, 2006.

905 Wilson, D. R., Smith, R. N. B., Gregory, D., Wilson, C. A., Bushell, A. C., and Cusack, S.: The large-scale cloud scheme
906   and saturated specific humidity, Unified Model documentation paper, 29, Met Office, Exeter, UK, 2007.

907 Wilson, D. R., Bushell, A. C., Kerr-Munslow, A. M., Price, J. D., Morcrette, C. J. and Bodas-Salcedo, A.: PC2: A prognostic
908   cloud fraction and condensation scheme. II: Climate model simulations, Q. J. R. Meteorol. Soc., 134(637), 2109–2125,
909   doi:10.1002/qj.332, 2008.

910 Winker, D. M., Vaughan, M. A., Omar, A., Hu, Y., Powell, K. A., Liu, Z., Hunt, W. H. and Young, S. A.: Overview of the
911   CALIPSO Mission and CALIOP Data Processing Algorithms, J. Atmos. Ocean. Technol., 26(11), 2310–2323,
912   doi:10.1175/2009JTECHA1281.1, 2009.

913 Wood, R.: Stratocumulus Clouds, Mon. Weather Rev., 140(8), 2373–2423, doi:10.1175/MWR-D-11-00121.1, 2012.

914 Wood, R. and Bretherton, C. S.: On the relationship between stratiform low cloud cover and lower-tropospheric stability, J.
915   Clim., 19(24), 6425–6432, doi:10.1175/JCLI3988.1, 2006.

916 Yamaguchi, T. and Randall, D. A.: Large-Eddy Simulation of Evaporatively Driven Entrainment in Cloud-Topped Mixed
917   Layers, J. Atmos. Sci., 65(5), 1481–1504, doi:10.1175/2007JAS2438.1, 2008.

918 Yukimoto, S., Yoshimura, H., Hosaka, M., Sakami, T., Tsujino, H., Hirabara, M., Tanaka, T. Y., Deushi, M., Obata, A.,
919   Nakano, H., Adachi, Y., Shindo, E., Yabu, S., Ose, T., and Kitoh, A.: Meteorological Research Institute Earth System
920   Model Version 1 (MRI-ESM1)—Model Description—, Tech. Rep. of MRI, 64, 83 pp, available at: http://www.mri-
921   jma.go.jp/Publish/Technical/index_en.html, 2011.

922   Yukimoto, S., Adachi, Y., Hosaka, M., Sakami, T., Yoshimura, H., Hirabara, M., Tanaka, T. Y., Shindo, E., Tsujino, H.,
923   Deushi, M., Mizuta, R., Yabu, S., Obata, A., Nakano, H., Koshiro, T., Ose, T., and Kitoh, A.: A new global climate
924   model of the Meteorological Research Institute: MRI-CGCM3 --Model Description and Basic Performance--, J.
925   Meteorol. Soc. Japan, 90A(0), 23-64, https://doi.org/10.2151/jmsj.2012-A02, 2012.

926   Yukimoto, S., Kawai, H., Koshiro, T., Oshima, N., Yoshida, K., Urakawa, S., Tsujino, H., Deushi, M., Tanaka, T., Hosaka,
927   M., Yabu, S., Yoshimura, H., Shindo, E., Mizuta, R., Obata, A., Adachi, Y. and Ishii, M.: The Meteorological Research
928   Institute Earth System Model version 2.0, MRI-ESM2.0: Description and basic evaluation of the physical component, J.
929   Meteor. Soc. Japan, 97, in press, https://doi.org/10.2151/jmsj.2019-051, 2019.

930   Zhang, Y., Xie, S., Covey, C., Lucas, D. D., Gleckler, P., Klein, S. A., Tannahill, J., Doutriaux, C. and Klein, R.: Regional
931   assessment of the parameter-dependent performance of CAM4 in simulating tropical clouds, Geophys. Res. Lett.,
932   39(14), 1–7, doi:10.1029/2012GL052184, 2012.

933   Zurovac-Jevtić, D. and Zhang, G. J.: Development and Test of a Cirrus Parameterization Scheme Using NCAR CCM3, J.
934   Atmos. Sci., 60(11), 1325–1344, doi:10.1175/1520-0469(2003)060<1325:DATOAC>2.0.CO;2, 2003.

935
936

937

Experiments	Section
Control (time step = 3600 s, 1800 s [default], 900 s, and 300 s)	
with an old version of stratocumulus scheme	3.1
with an old treatment of the WBF effect	3.2
shallow convection can be active even under stratocumulus conditions	3.3
shallow convection can be active even under stratocumulus conditions using L48	3.4
with an old version of cloud overlap scheme	3.5
radiation calculation for every two latitudinal grids	3.6
1-hourly longwave radiation calculation	3.6
using original (not doubled) number concentration of sea salt CCN	3.8
with an old version of ice fall scheme (time step = 3600 s, 1800 s, 900 s, and 300 s)	3.9

938

939 **Table 1: List of sensitivity experiments performed in the present study using MRI-ESM2 to identify the effect of each modification.**
940 **The second column shows the section in which each modification is discussed.**

941

942

943

944

945
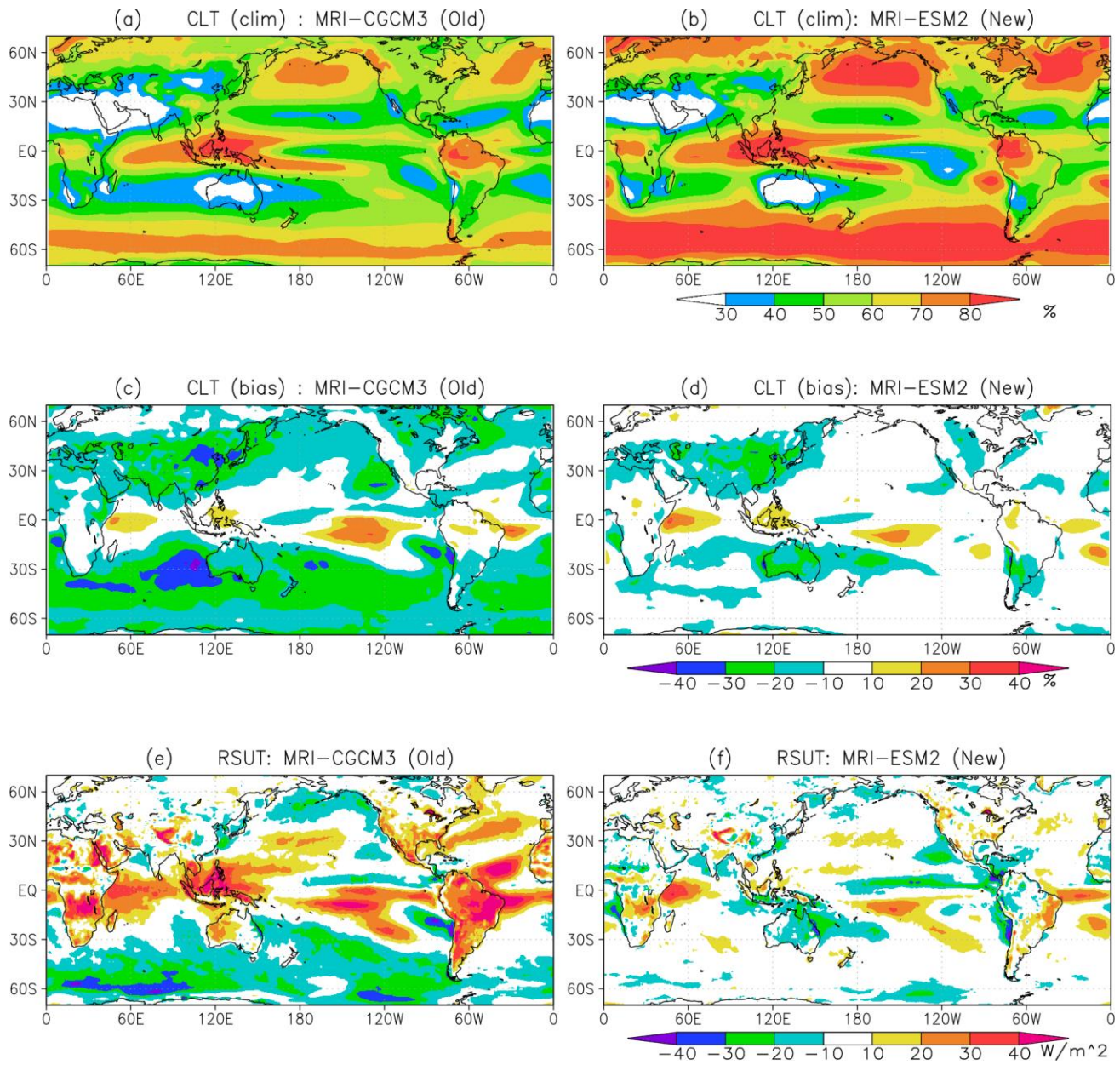
Figure 1: (a, b) Climatologies of total cloud cover (%), (c, d) biases of total cloud cover (%) with respect to ISCCP observations, and (e, f) biases of upward shortwave radiative flux (W m⁻²) at the top of the atmosphere with respect to CERES-EBAF simulated by (a, c, e) MRI-CGCM3 and (b, d, f) MRI-ESM2. The climatologies cover the period 1986–2005 for model simulations and ISCCP observational data, and 2001–2010 for CERES-EBAF data.

946
947
948
949
950
951
952
953

954

955
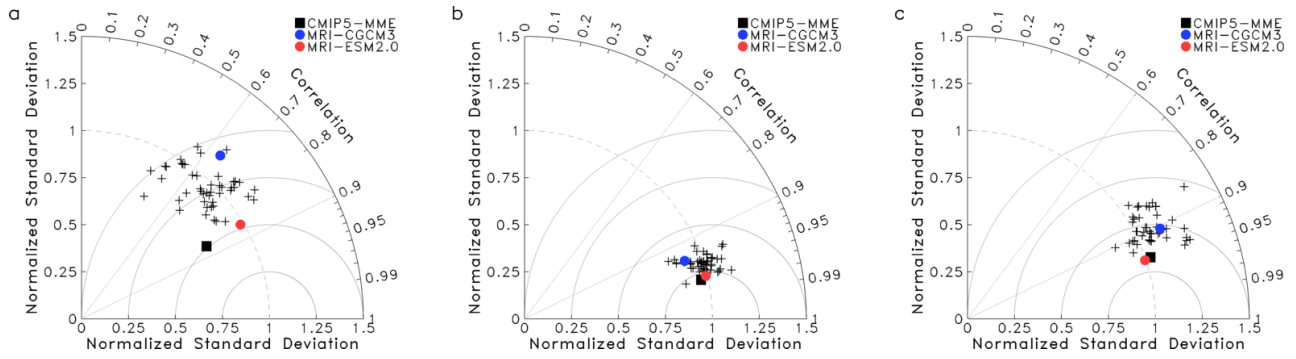
Figure 2: Taylor diagrams for upward (a) shortwave, (b) longwave, and (c) net radiative fluxes at the top of the atmosphere for MRI-CGCM3 (blue dot), MRI-ESM2 (red dot), the CMIP5 multi-model mean (black square), and individual CMIP5 models (crosses). CERES-EBAF data are used as observations.

959

960

961
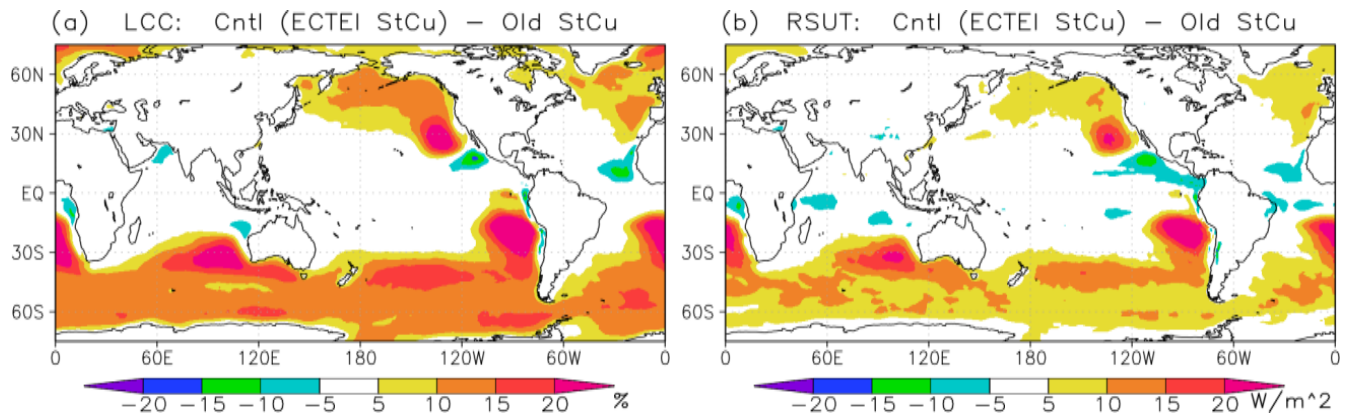
Figure 3: Impacts of the new stratocumulus scheme on (a) low cloud cover (%) and (b) TOA upward shortwave radiative flux (W m^{-2}). The plots show results for the control model (with the new stratocumulus scheme) minus those for an experiment with an old version of the stratocumulus scheme.

973

974
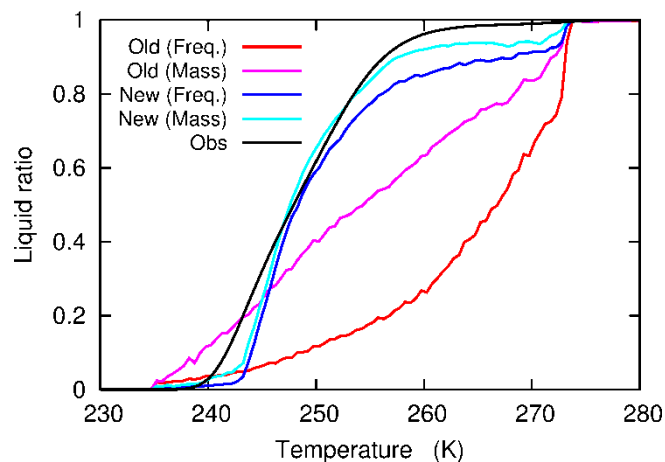
Figure 4: Ratio of super-cooled liquid water to total cloud water as a function of temperature. The plot is obtained from snapshot global data for 10 days in July 2001 using the old (red and pink lines) and new (blue and light blue lines) treatments of the WBF effect. The ratios are calculated using two methods: mass weighted ratio (pink and light blue lines) in which liquid and ice masses are averaged over temperature bins first and the liquid water ratio is calculated from the averaged masses, and frequency ratio (red and blue lines) in which the snapshot ratio of liquid water is weighted by snapshot cloud fraction and averaged over temperature bins. An observational curve from Hu et al. (2010) that corresponds to a frequency ratio is also shown (black line).

981

982

983

984

985

986
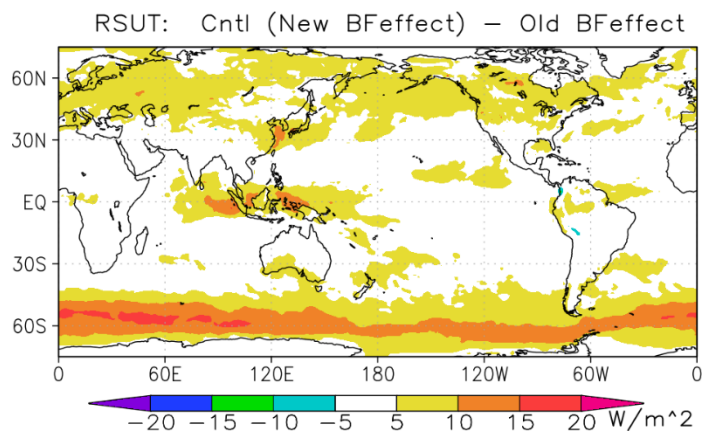
Figure 5: Impact of the new treatment of the WBF effect on TOA upward shortwave radiative flux (W m⁻²). The plot shows the results for the control model (with the new treatment) minus those for an experiment with an old version of the treatment.

989

990

991

992

993

994
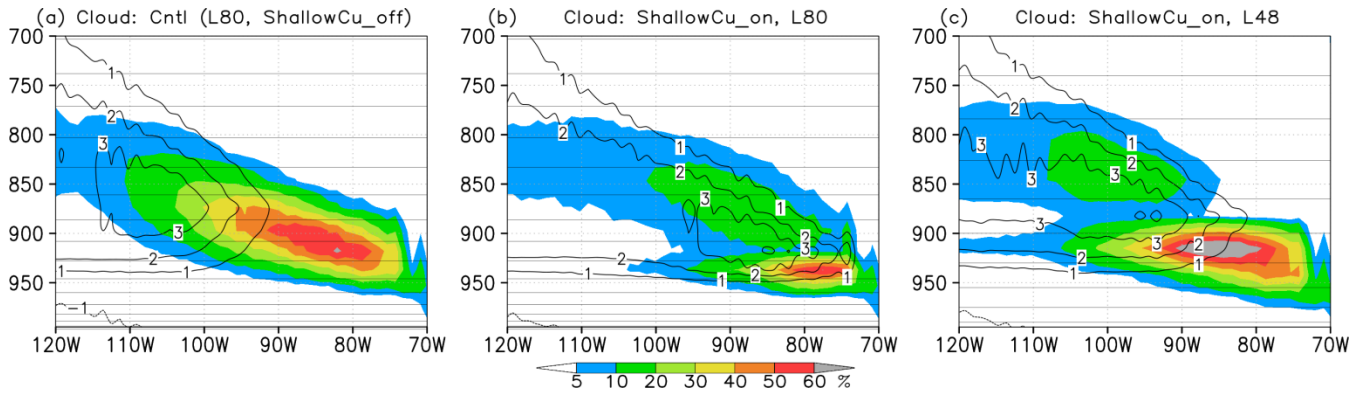
Figure 6: Cross sections of cloud fraction (colour, %) along 20°S for January. (left) The control model (L80, a treatment of shallow convection suppressed under stratocumulus conditions), (middle) the same as the left panel but where shallow convection can be active even under stratocumulus conditions, and (right) the same as the middle panel except for vertical resolution L48. Horizontal straight lines show the vertical model layers and contours show the heating rate of the convection scheme (K day^{-1}).

999

1000

1001

1003
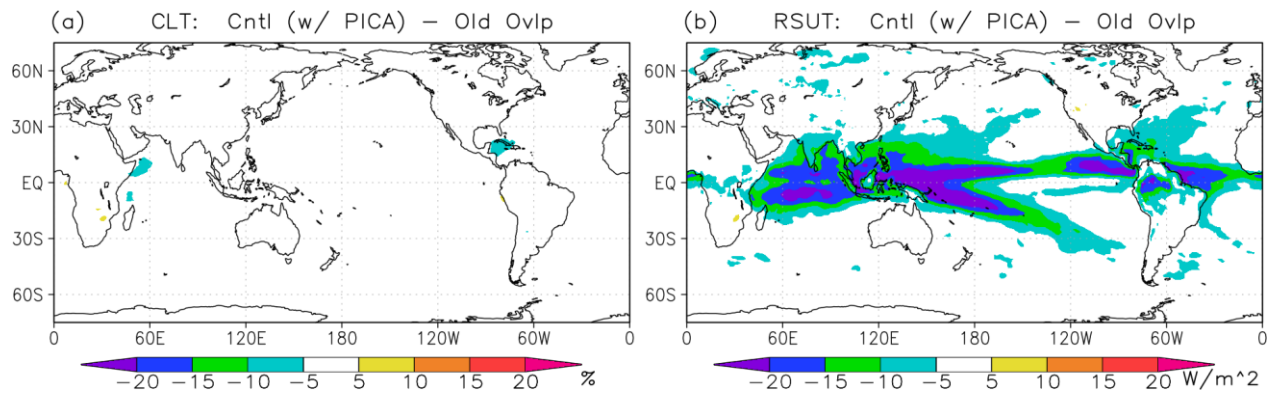
1004

Figure 7: Impacts of new cloud overlap scheme, PICA, for shortwave radiation calculation on (a) total cloud cover (%) and (b) TOA upward shortwave radiative flux (W m^{-2}). The plots show results for the control model (with PICA) minus those for an experiment with an old version of the cloud overlap scheme.

1008

1009
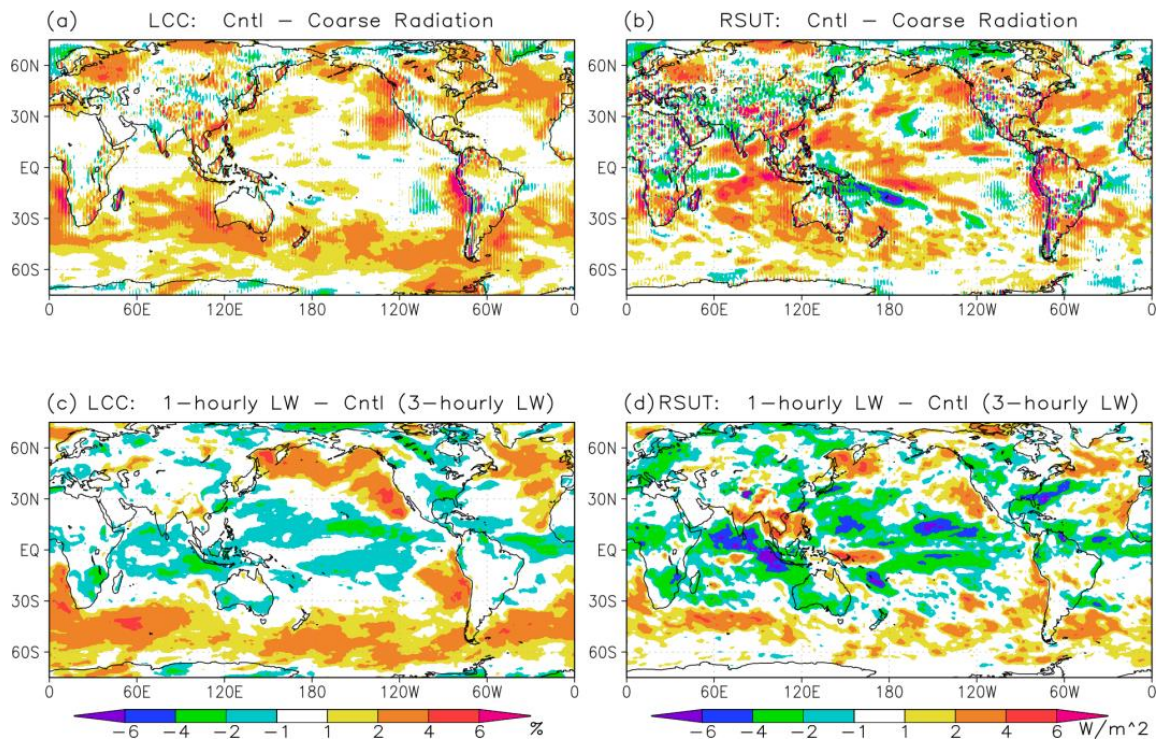
Figure 8: Impacts of (a, b) increased horizontal resolution for the radiation calculation and (c, d) increased frequency of calculation for longwave radiation on (a, c) low cloud cover (%) and (b, d) TOA upward shortwave radiative flux (W m^{-2}). Panels (a, b) show results for the control model (calculation for every single grid box) minus those for an experiment with calculation for every two latitudinal grid boxes. Panels (c, d) show results for an experiment with 1-hourly longwave radiation calculation minus those for the control model (3-hourly calculation).

1020
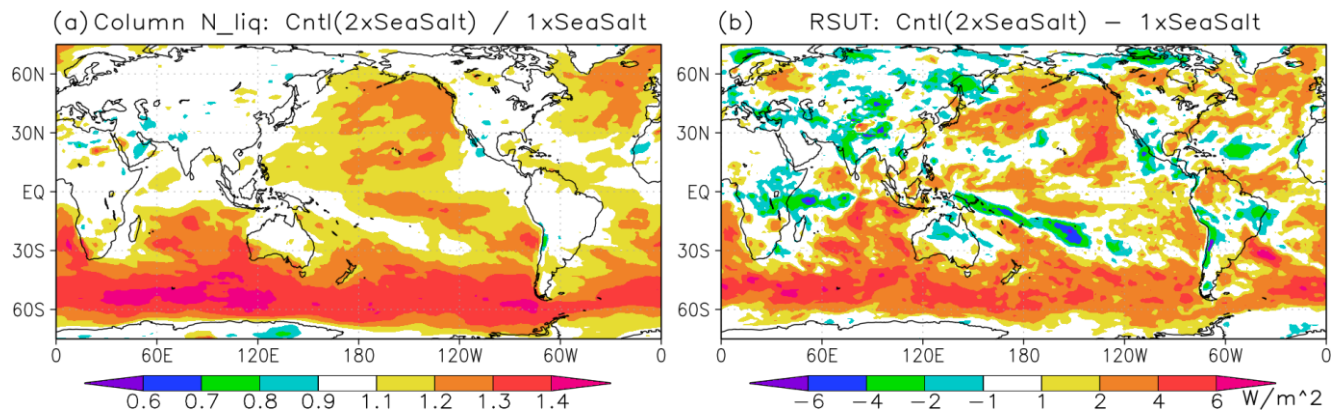
1021

1022

1023 **Figure 9: Impacts of doubled number concentration of sea salt CCN on (a) column-integrated number concentration of cloud**
1024 **droplets (unitless) and (b) TOA upward shortwave radiative flux (W m^{-2}). The panels show the ratio (a) and the difference (b)**
1025 **between results for the control model (doubled number concentration of sea salt CCN) and those for an experiment using the**
1026 **original number concentration of sea salt CCN.**
1027

1028

1029
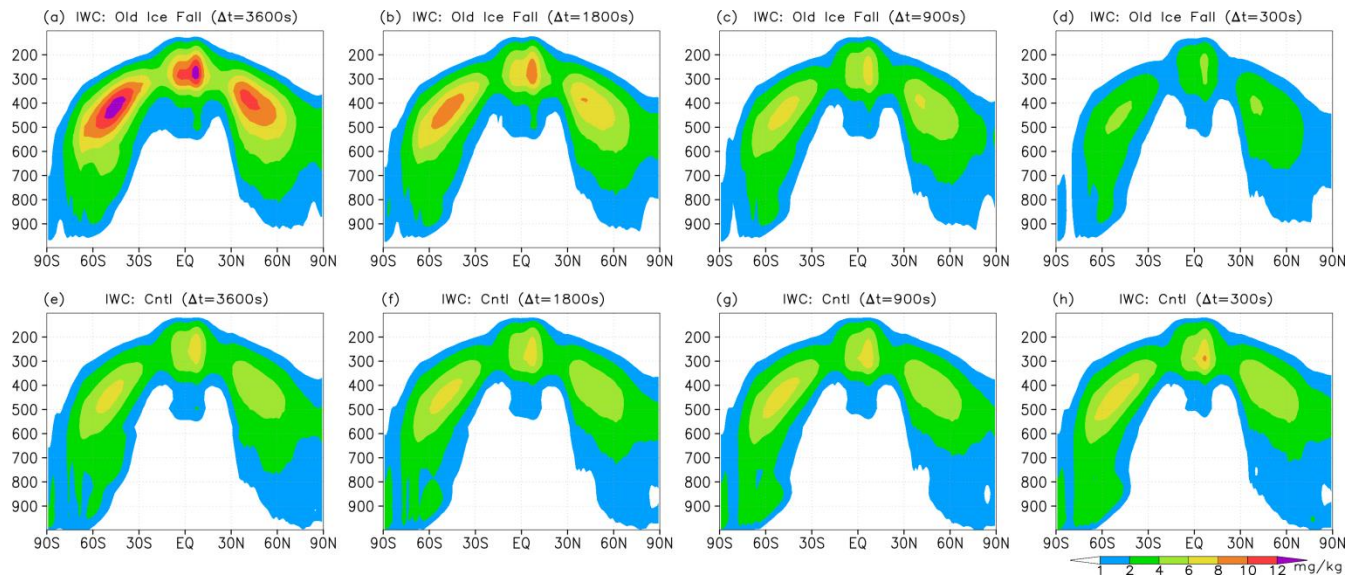
1030

1031

1032 **Figure 10: Zonal average of ice water content (mg kg⁻¹) for different model time steps. Upper panels show results using the old ice**
1033 **fall scheme and lower panels the control simulation using the modified ice fall scheme. From left to right, the time steps are 3600 s,**
1034 **1800 s, 900 s and 300 s. The vertical axis shows air pressure (hPa) and the horizontal axis shows latitude.**
1035

1036

1037
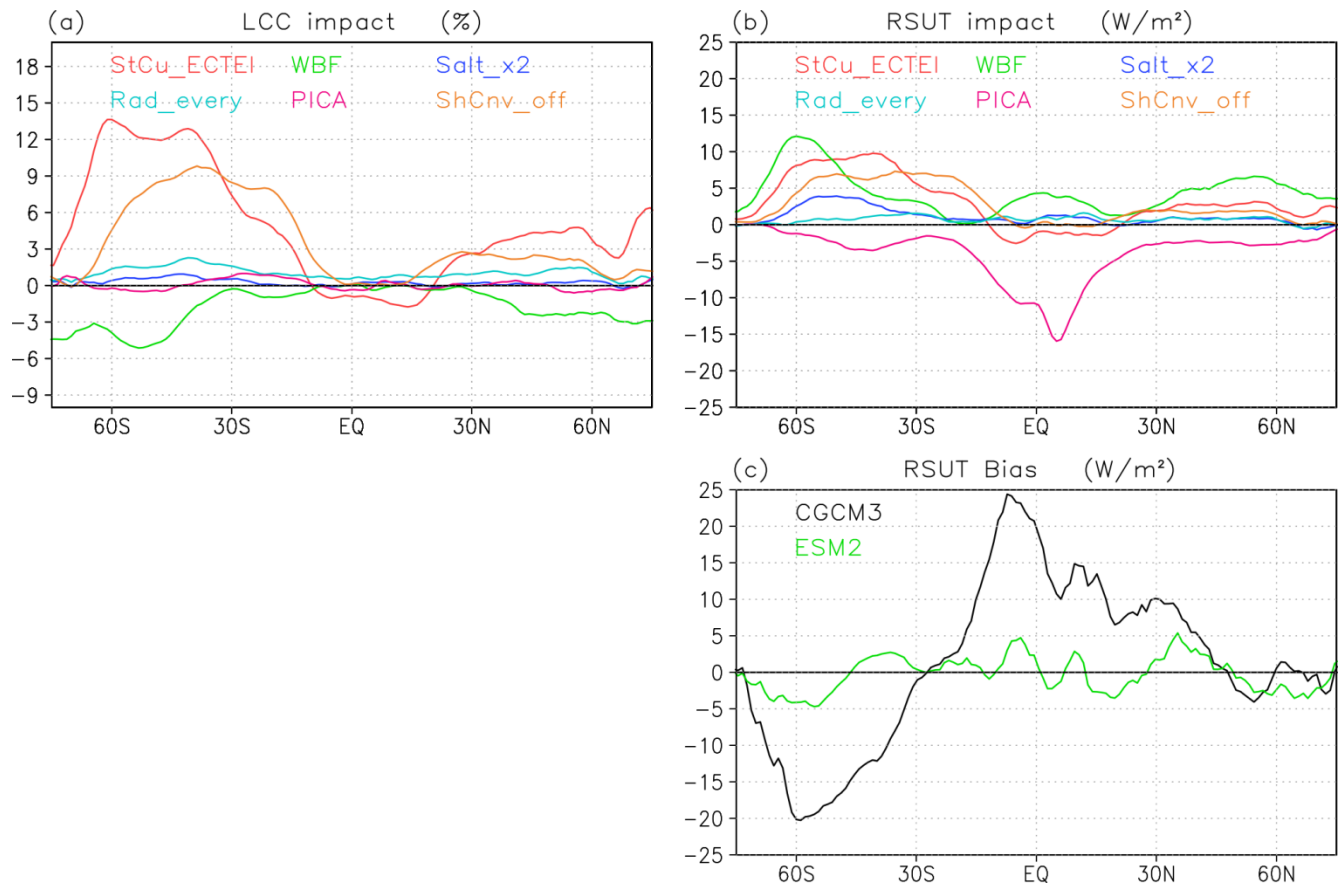
1038

1039

1040 **Figure 11: Impacts of each modification on zonal means of (a) low cloud cover (%) and (b) TOA upward shortwave radiative flux**
1041 **(W m⁻²). Modifications include a new stratocumulus scheme (red line), the new treatment of the WBF effect (green), doubled**
1042 **number concentration of sea salt CCN (blue), increased horizontal resolution for radiation calculation (light blue), a new cloud**
1043 **overlap scheme, PICA (pink), and a treatment of shallow convection suppressed under stratocumulus conditions (orange). Each**
1044 **impact is calculated from the simulation data described in Section 2.3. The biases in TOA upward shortwave radiative flux for**
1045 **MRI-CGCM3 (black line) and MRI-ESM2 (green) are also shown in panel (c), where the data used are the same as in Fig. 1.**

1046
1047

1048
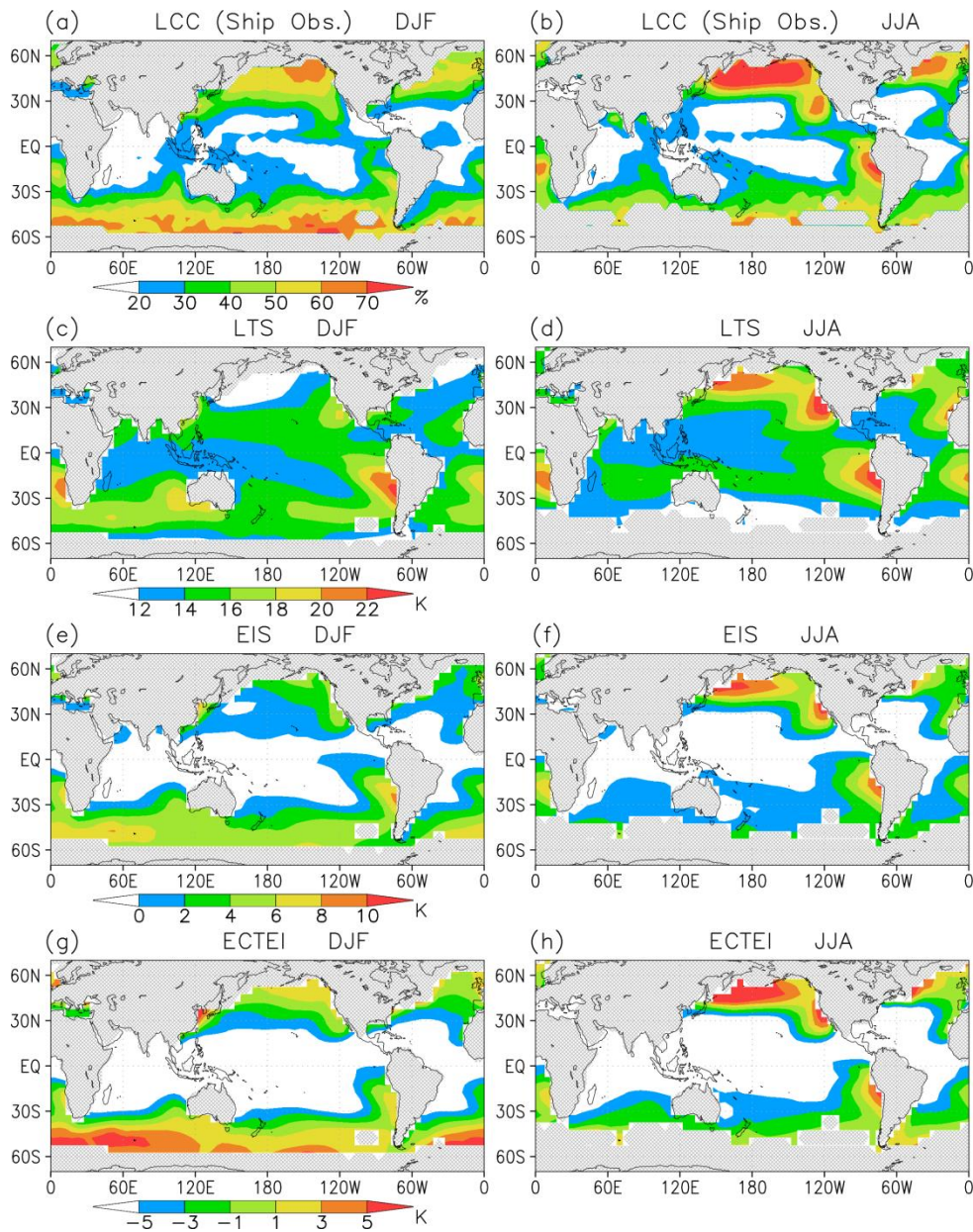
1049

1050
Figure 12: Climatologies of low stratiform cloud cover (%), LTS (K), EIS (K), and ECTEI (K) for December to February (left panels) and June to August (right panels). Cloud cover data were obtained from EECRA shipboard observations and stability indexes were calculated using ERA-40 data (1957–2002).

1054
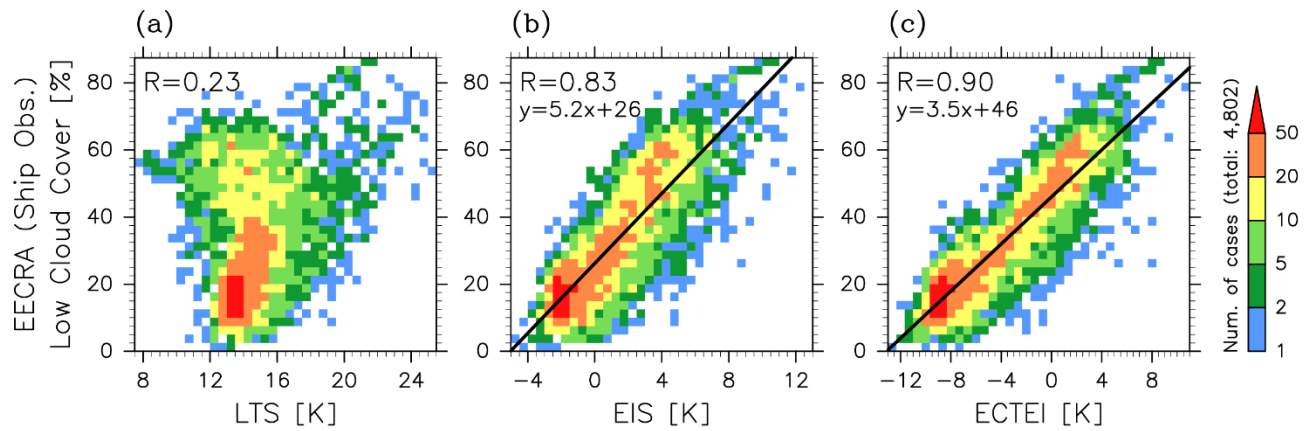
Figure 13: Frequencies of occurrence of low stratiform cloud cover (combined cloud cover of stratocumulus, stratus, and sky-obscuring fog) sorted by (a) LTS, (b) EIS, and (c) ECTEI ($\beta = 0.23$), based on all 5° × 5° seasonal climatology data. Data are the same as in Fig. 12 but all the data between 60°N and 60°S for all seasons were used. Linear regression lines and the correlation coefficients are shown.
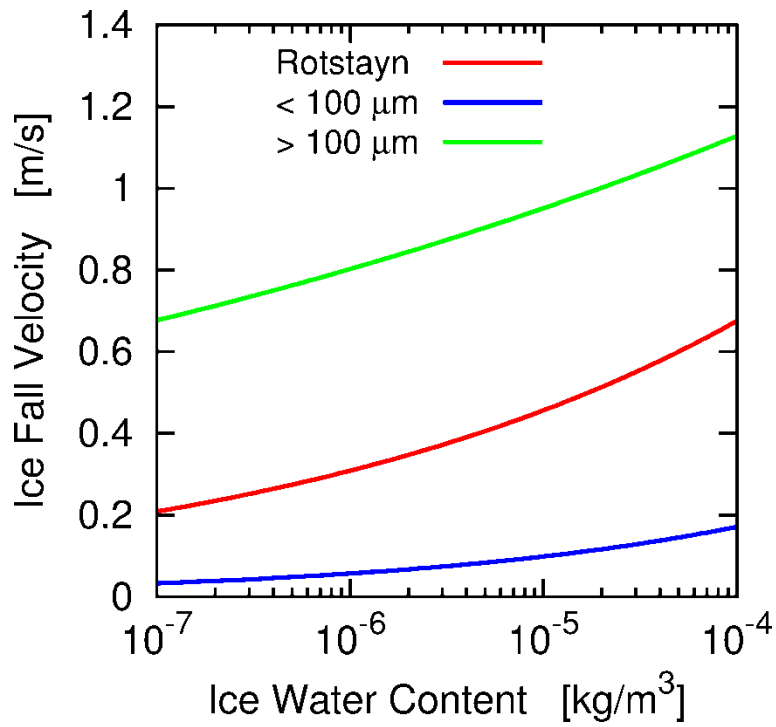
1067 **Figure 14: Ice sedimentation velocities (m s⁻¹) of Rotstayn (1997) (Eq. (1), red line), derived for particles smaller than 100 µm (Eq.**
1068 **(3), blue line), and for particles larger than 100 µm (Eq. (4), green line). The horizontal axis shows ice water mass density $\rho_a\, q_i$**
1069 **(kg m⁻³).**
1070
1071